

Finding Halos in the Lyman- α Forest

Duarte Muñoz Santos¹, Matthew M. Pieri¹, Dylan Nelson², Teng Hu¹, Simon Weng¹, and Manuel F. Ruiz-Herrera Bernal^{3,4}

¹ Aix Marseille Univ, CNRS, CNES, LAM, Marseille, France

E-mail: duarte.santos@lam.fr

² Universität Heidelberg, Zentrum für Astronomie, ITA, Albert-Ueberle-Str. 2, 69120 Heidelberg, Germany

³ CIEMAT, Avenida Complutense 40, E-28040 Madrid, Spain

⁴ Facultad de Físicas, Universidad de Sevilla, Avda. Reina Mercedes s/n, Campus de Reina Mercedes, 41012 Sevilla, Spain

Received ?? Accepted ??

ABSTRACT

It has been demonstrated that one can track down galaxies in absorption ‘hidden’ in the Lyman- α forest through the use of ‘strong, blended Lyman- α ’ (or SBLA) absorption. Specifically a series of publications studied SBLA absorption systems with Lyman- α flux transmission, $F_{\text{Ly}\alpha} < 0.25$ on scales of 138 km s^{-1} in the Sloan Digital Sky Survey (SDSS). In order to better understand the connection between halos and these SBLAs, we make use of several million synthetic absorption spectra from the TNG50 cosmological simulation, at $z = 2$ and $z = 3$. We explore spectra with SDSS-like resolution in order to understand the nature of SBLAs as defined thus far, as well as with high resolution (or ‘resolved’) spectra to generalise and optimise SBLAs as halo finders. For the SDSS SBLAs, we find that up to 78% of these absorption systems reside in halos, where the stronger the absorption and the lower the redshift, the higher the probability. We also manage to recover a mean halo mass of $10^{12.25} M_{\odot}$, in line with what is measured in observations. For the resolved SBLAs, we expand on the previous definition and allow the SBLA spectral size to vary between 54 km s^{-1} and 483 km s^{-1} . We find that the largest absorbers have the highest probability of finding halos. When applying a hierarchical framework, where we allow the largest SBLAs to consume the smaller ones, we find that the halo mass distributions for each SBLA spectral size becomes narrower with respect to the non-hierarchical case. We are also able to probe halo masses from $M_h \approx 10^{9.5} M_{\odot}$ (for 100 km s^{-1} SBLAs) to $M_h \approx 10^{11.5} M_{\odot}$ (for 450 km s^{-1} SBLAs). With these results, we show that we are able to transform the Lyman- α forest into a powerful halo finding machine for not only identifying CGM regions, but also estimating their host halo masses.

Key words. Galaxies: evolution - Galaxies: intergalactic medium - Quasars: absorption lines - Cosmology: theory - Techniques: spectroscopic - Methods: numerical

1. Introduction

Ever since the ‘Great Debate’ (Shapley & Curtis 1921; Hoskin 1976), the existence of ‘island universes’ has shaped our view of the Universe. Now, after a little over a century, we have come to a new understanding that these objects, which we now call galaxies, are pieces of the puzzle that help us understand the history of the Universe. By tracing their formation and evolution, we can better understand how we have reached our current epoch.

Galaxies are not isolated systems, however. They are a part of the tangled cosmic web of the Universe, interacting not only with each other (e.g. Messier 51, Toomre & Toomre 1972), but also with the medium around them (e.g. Bergeron & Stasińska 1986). Understanding the relationship between the intergalactic medium (IGM) and galaxies allows us to paint a picture of how galaxies form and evolve. The IGM contributes pristine gas for star-formation, while galaxies eject metals into the IGM via outflows driven by active galactic nuclei (AGN) or stellar feedback (Tinsley 1980; Lilly et al. 2013; Dekel & Mandelker 2014).

After the discovery of quasars by Schmidt (1963), the analysis of the restframe ultraviolet spectra of these objects revealed a trough in absorption (Gunn & Peterson 1965). However, with higher resolution spectra, a ‘forest’ of absorption blueward of the Lyman- α emission line was revealed, first described as a set of discrete clouds in the IGM (Bahcall & Spitzer 1969), but nowadays as a fluctuating density field of neutral hydrogen gas, or the

fluctuating Gunn-Peterson approximation (e.g. Croft et al. 1998; Weinberg et al. 2003). This allows us to, for example, trace the properties of the medium between galaxies such as density, temperature and metallicity (e.g. Hu et al. 2025).

This interface between galaxies and the IGM is called the circumgalactic medium (CGM), typically defined as the region that starts from the galactic disc and extends up to the virial radius (e.g. Tumlinson et al. 2017). This is one of the main baryonic reservoirs of the Universe, so understanding its relationship with galaxies and the IGM, as well as how it has changed and evolved with time is of crucial importance. There are many methods to observe and analyse this medium, ranging from direct emission line maps (e.g. Lusso et al. 2019; Martin et al. 2023; Tornotti et al. 2025), to ‘down the barrel’ spectroscopy (e.g. Henry et al. 2015; Heckman et al. 2015), but by far the most common is through absorption-line spectroscopy.

Although the diffuse IGM is traced by the Lyman- α forest, it is not exclusively created by diffuse gas. When lines-of-sight pass through the CGM, Lyman- α forest absorption may also be generated (Lanzetta et al. 1995; Barcons et al. 1995; Chen et al. 1998).

The standard way to trace galaxies in quasar absorption spectra is through high hydrogen column density systems, from Damped Lyman- α (DLA) systems ($N_{\text{HI}} \gtrsim 10^{20} \text{ cm}^{-2}$, e.g. Wolfe et al. 2005; Chen et al. 2005; Péroux et al. 2022; Weng et al. 2023; Nuñez et al. 2024), or Lyman Limit Systems (LLS,

$10^{17} \text{ cm}^{-2} \lesssim N_{\text{HI}} \lesssim 10^{20} \text{ cm}^{-2}$, e.g. Fumagalli et al. 2013; Lehner et al. 2013), but in reality a wider range of gas conditions, and therefore column densities, are present in the CGM. Simulations such as Hummels et al. (2019) and Oppenheimer et al. (2020) show that a large fraction of the CGM ($\gtrsim 90\%$) is made up of lower column density systems ($N_{\text{HI}} \lesssim 10^{17} \text{ cm}^{-2}$). Furthermore, in the simulations studied here, only about 1.2% of the Lyman- α forest is associated with the CGM. By only using DLAs and LLS (as well as their subclasses) we are limiting ourselves to only a biased subset of CGM systems and an order of magnitude fewer systems than is traced in absorption.

Using data from the Sloan Digital Sky Survey (SDSS, Fukugita et al. 1996; Gunn et al. 1998; York et al. 2000), Pieri et al. 2010 (hereafter P10) and Pieri et al. 2014 (hereafter P14) found that absorbers with Lyman- α flux transmission below 25% and on 138 km s^{-1} scales in the forest are typically associated with optically thin CGM gas. Afterwards, Morrison et al. 2024 (hereafter M24) explored their properties in more detail and proposed to name them strong, blended Lyman- α (SBLA). They stacked their restframe spectra, with $\langle z \rangle = 2.7$, and were able to provide insights into the density and metallicity of different phases of the CGM. Particularly, studying the low-ionisation species found that there appears to be sub-parsec scale clumping. This is not the only method to detect the CGM through absorbing structures – another example comes from the MAMMOTH project (MApping the Most Massive Overdensity Through Hydrogen, Cai et al. 2016, 2017), where strong absorption over large scales ($15 - 30 \text{ Å}$ at $z = 2.5$, or about $1025 - 2143 \text{ km s}^{-1}$, in $15 - 30 h^{-1} \text{ Mpc}$ scales) is associated with Lyman- α emitters.

SBLAs, then, are an useful alternative when compared with their higher column density counterparts because: they are numerous (incidence rate of 12.4; M24), especially when compared to DLAs or LLS (incidence rates of 0.06 and 1.21, respectively; Prochaska et al. 2005; Fumagalli et al. 2013); trace many phases of the CGM; and provide insights into the structure of the medium. Despite this, little is known about their novel selection, and answering questions about, for example, how often they trace galaxies as opposed to clusters of IGM absorbers, is particularly difficult with observations. In P14, a small number of Lyman break galaxies near quasar lines-of-sight were studied, but overall the information provided by observations is severely limited by the small samples of galaxies currently available above $z = 2$ with associated CGM information.

In this paper, we wish to explore how SBLAs can be used to find galaxies at $z > 2$. We use the TNG50 simulation (Pillepich et al. 2019; Nelson et al. 2019) as a model universe to build greater insight into these objects. With this simulation, we can assess how effectively SBLAs (as defined by M24) trace the CGM. Indeed we can go further and ask whether we can refine the definition of SBLAs in order to improve the fidelity of CGM recovery.

This paper is structured as follows: in Sect. 2 we briefly describe the TNG50 simulation, as well as what data we use from it; in Sect. 3 we describe the selection process of SBLAs, and how we associate them with halos; in Sect. 4 we show the results of SBLAs that have the same properties as M24; in Sect. 5 we explore modifications to the SBLA definition for a range of absorption blend sizes and their characteristic masses. We then build a hierarchical scheme for building a sample of SBLAs of varying sizes to reflect a range of halo masses; in Sect. 6 we discuss our results and in Sect. 7 we provide our conclusions.

2. Hydrodynamic Simulations and Synthetic Spectra

This work uses TNG50¹ (Pillepich et al. 2019; Nelson et al. 2019), the highest-resolution version of the IllustrisTNG suite of large-scale cosmological magneto-hydrodynamical simulations (Marinacci et al. 2018; Naiman et al. 2018; Nelson et al. 2018; Pillepich et al. 2018a; Springel et al. 2018). IllustrisTNG was built upon the foundation of the original Illustris simulation (Genel et al. 2014; Vogelsberger et al. 2014a,b; Sijacki et al. 2015), now incorporating magnetic fields (Pakmor et al. 2014) and with changes on the original galaxy formation model (Vogelsberger et al. 2013; Torrey et al. 2014) through the introduction of updated feedback mechanisms (Weinberger et al. 2017; Pillepich et al. 2018b). As the name implies, the TNG50 simulation spans roughly 50 comoving Mpc (cMpc), or 35 cMpc/h, with $H_0 = 67.74 \text{ km s}^{-1} \text{ Mpc}^{-1}$ and a cosmology of $\Omega_0 = 0.3089$ and $\Omega_\Lambda = 0.6911$, and has a resolution comprising 2160^3 elements, attaining a baryonic (dark matter) mass resolution of $8.5 \times 10^4 M_\odot$ ($4.5 \times 10^5 M_\odot$). The combination of a substantial volume and high spatial resolution makes it particularly well-suited for examining the CGM of galaxies. We considered the simulation box at two redshifts: $z = 2$ and $z = 3$, in order to study how the absorber-halo relationship is affected by different epochs of the Universe.

We made use of 4 million parallel line-of-sight noiseless synthetic transmission spectra that are randomly spread across the TNG50 simulation box and include only the Lyman series transition lines (Nelson et al. in prep.). In the Lyman- α transition, this equates to a minimum wavelength of 3645 Å and 4870 Å , and a maximum wavelength of 3695 Å and 4930 Å , for $z = 2$ and $z = 3$, respectively.² Hereafter when we use the term ‘lines-of-sight’ it should be noted that we refer to these short stretches of absorption spectrum and not the hundreds of ångströms typically observed in Lyman- α forest quasars. In order to calculate the ionisation state of hydrogen, the ultraviolet background from Faucher-Giguère et al. (2009) was used; the HI density was estimated based on the neutral hydrogen abundance computed during the actual simulation, which uses on-the-fly self-shielding based on the Rahmati et al. (2013) model – this is re-computed for dense, star-forming gas in post-processing; and the molecular H₂ was removed using the pressure-based model of Blitz & Rosolowsky (2006).

We study these synthetic spectra with two resolutions: SDSS-BOSS-like resolution (69 km s^{-1}) and KECK/HIRES-like resolution (4.5 km s^{-1}). Since the specific resolution of HIRES spectra is not impactful in this study, we refer to this sample hereafter as ‘resolved spectra’. See Fig. 1 for an example of a resolved spectrum, with a halo marked.

We extracted properties from the halos present in the simulation, namely: the three dimensional position of the centre of mass of halos; R_{vir} is the virial radius of halos, which we define as the comoving radius of a sphere centred on a halo where the mean overdensity is $\rho/\bar{\rho} = 200$, where $\bar{\rho}$ is the mean density of the Universe; M_h is the mass of each halo; and v_{pec} is the peculiar velocity of the halo. We also considered the theoretical value for the maximum circular velocity of each halo which we define as:

$$v_{200} = \sqrt{\frac{GM_{200}}{R_{\text{vir}}}} \quad (1)$$

¹ <https://www.tng-project.org/data/>

² This translates into wavelength intervals of about 50 Å per spectrum for $z = 2$ and about 60 Å per spectrum for $z = 3$.

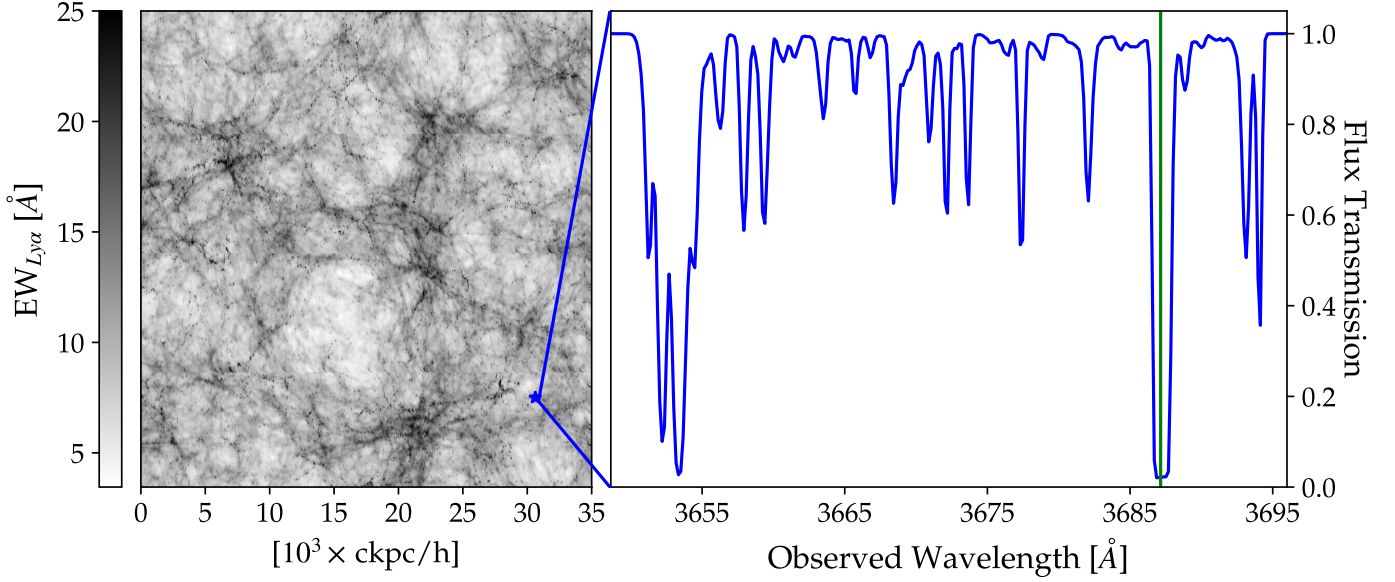


Fig. 1. A randomly-selected resolved spectrum (right) from the TNG50 simulation box (left). The spectrum has the ‘resolved’ resolution at $z = 2$, whose position is denoted by the blue star on the left. Only the Lyman- α transitions are shown. In the box coordinates, the x- and y-axis have the same dimensions, and this data is taken from the evenly sampled lines-of-sight list, with a spacing of 35 ckpc/h. The colourbar represents the integrated equivalent width (EW) of the Lyman- α transition for each spectrum. The green vertical line marks the position of a halo in the spectrum.

where M_{200} represents the mass of the halo defined when $\rho/\bar{\rho} = 200$, and R_{vir} its associated virial radius.

In order to make the statistics of our synthetic absorption spectra as realistic as possible, we post-process them as follows. First, we rescale their mean optical depth at each redshift to match the observed value (following Eq. 21 of [Faucher-Giguère et al. 2008](#)). In order to do this, we performed the global mean of the optical depth of all spectra at each redshift, and then divided it with the observed value. Afterwards, we took this factor and multiplied it with the optical depth of each individual spectrum so that the rescaling could be done. Secondly, we remove all the lines-of-sight that include Damped Lyman- α (DLA) or sub-DLA absorbers, so they do not contaminate our sample of SBLAs. To do this, we conservatively selected the lines-of-sight that have integrated hydrogen column density $N_{HI} > 10^{19} \text{ cm}^{-2}$, accounting for 81 733 lines-of-sight at $z = 2$ and 204 815 lines-of-sight at $z = 3$ – this is equivalent to 2% and 6%, respectively, of the total available lines-of-sight.

3. SBLA Detection and Halo Matching

In the previous section we provided details about the TNG50 simulation and the synthetic spectra we will be using in this work. Here, we explore how we select SBLAs, and how we associate them with halos. In Fig. 2 we can see a series of nearby transmission spectra that probe a region around two halos: one of mass $10^{11.54} M_{\odot}$ (represented in red) and another of mass $10^{10.04} M_{\odot}$ (represented in yellow). These halos are shown in one spatial direction and in the line-of-sight direction for the native spectral resolution, including different spectral bin sizes. In binned cases we mask everything except flux transmission below 25% to illustrate the SBLA selection on different scales.

In Sect. 4 we will explain in more detail their selection with SDSS-like data, and set about exploring what simulations tell us about them. In Sect. 5 we will explore a more general definition of SBLAs, using the resolved spectra.

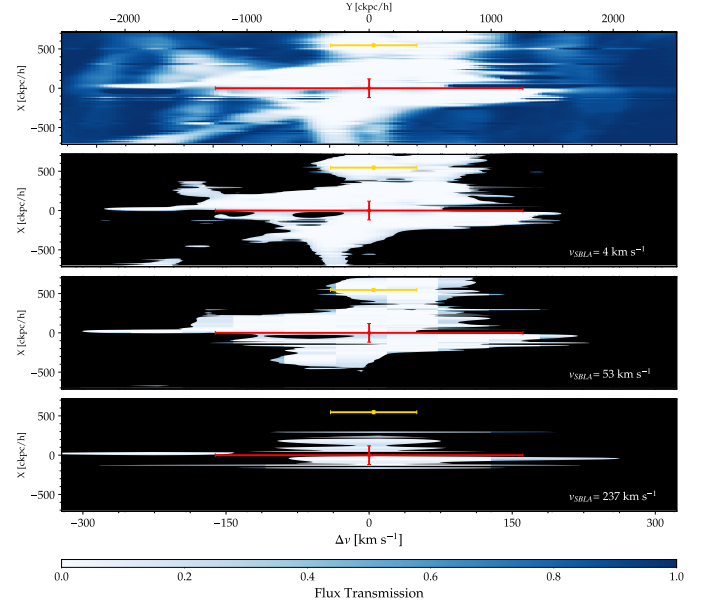


Fig. 2. Representation of two halos in physical and line-of-sight dimensions. On the y-axis and the top x-axis, we have the physical dimensions, and on the bottom x-axis, we have the line-of-sight direction. The red lines represent a halo of mass $10^{11.54} M_{\odot}$ and the yellow lines represent a halo of mass $10^{10.04} M_{\odot}$. The top panel represents the Lyman- α flux transmission without restrictions, as shown on the bottom colourbar. The bottom three panels represent a limit on the flux transmission of 25%, with the binning of the spectrum, v_{SBLA} , increasing from top to bottom: 4 km s $^{-1}$, 53 km s $^{-1}$ and 237 km s $^{-1}$.

We will now define the framework we use for spatially and spectrally associating SBLAs with halos. We considered three criteria to achieve this: 1) halos must have masses above $10^9 M_{\odot}$,

2) the line-of-sight hosting the SBLA should pass within the R_{vir} of the halo, and 3) the spectral range associated with the SBLA must overlap with the spectral range in the Lyman- α forest described by the redshift and the circular velocity of the halo.

For point 2) to be true, we apply a simple condition, where he have that:

$$(X_{\text{SBLA}} - X_{\text{Halo}})^2 + (Y_{\text{SBLA}} - Y_{\text{Halo}})^2 \leq R_{\text{vir}}^2 \quad (2)$$

where X_{SBLA} and Y_{SBLA} represent the positions of the lines-of-sight that hold SBLAs and X_{Halo} and Y_{Halo} represent the positions of the halo, in the simulation box.

For point 3) to be true, we need to ensure that the redshift difference between the halo and the SBLA, expressed as a velocity, is less than the halo circular velocity. In other words:

$$\Delta v = c \frac{|z_{\text{SBLA}} - z_{\text{Halo}}|}{1 + z_{\text{Halo}}} \leq v_{200} \quad (3)$$

where c represents the speed of light in km s^{-1} , z_{SBLA} represents the redshift of the SBLA, z_{Halo} represents the redshift of the halo and v_{200} the halo circular velocity defined in Eq. 1.

4. SDSS-like SBLAs

In this section, we explore SBLAs found as defined in the literature (P10, P14 and M24), using the SDSS-like synthetic spectra. To do so, we must first obtain our SBLA sample, following the lead of these previous works.

We rebinned our SDSS-like spectra by 2 pixels, which translates into an SBLA spectral size of $v_{\text{SBLA}} = 138 \text{ km s}^{-1}$. We use the standard definition of SBLAs stated in M24 that the noiseless flux transmission must be $F_{\text{Ly}\alpha} < 0.25$. We explore SBLAs in greater detail by introducing more selective samples, limited to stronger absorption ($F_{\text{Ly}\alpha} < 0.15$ and $F_{\text{Ly}\alpha} < 0.05$). While these three tiers may appear similar to the FS0, FS1 and FS2 samples of M24, our samples are different since they do not include the noise-in samples with the associated purity and completeness of SBLA finding (in order to understand the relationship between idealised noiseless SBLAs and real samples see Fig. 3 of P14). Furthermore, we calculated the incidence rates of SBLAs, which we explain with more detail in Appendix A.

Depending on the flux limits, we find between 10^3 to 10^5 SBLAs at $z = 2$, and 10^5 to 10^6 SBLAs at $z = 3$, with the highest flux limit ($F_{\text{Ly}\alpha} < 0.25$) possessing the largest number of these objects. Overall, we find that between 0.03% – 2.9% of spectra have SBLAs at $z = 2$, while at $z = 3$ we have between 3% – 37%. This does not take into the account the spectra with DLAs.

4.1. Total Probability for SDSS SBLAs

Following the procedure laid out in Sect. 3 to associate SBLAs with halos, we can then define the total probability of finding an SBLA inside a halo as P_{tot} , seen in Eq. 4.

$$P_{\text{tot}} = \frac{\text{Number of SBLAs in halos}}{\text{Total number of SBLAs}} \quad (4)$$

SBLAs with $v_{\text{SBLA}} = 138 \text{ km s}^{-1}$ are found inside halos with P_{tot} values that range between 17 – 78%, depending on how restrictive we are with the flux limits and the redshift considered (see Table A.2 for more details).

Unsurprisingly, the highest probabilities come from the cases with the lowest flux limit: 78% for $z = 2$ and 42% at $z = 3$. The

standard SBLA definition ($F_{\text{Ly}\alpha} < 0.25$) implies a halo finding probability of 56% and 17% for $z = 2$ and $z = 3$, respectively. This is broadly consistent with the estimate in P14 that $\approx 60\%$ of SBLA with $2.1 < z < 3$ are near Lyman break galaxies.

4.2. Halo Mass Dependence for SDSS SBLAs

P_{tot} is a useful metric for how SBLAs are tracing halos (and so, CGM regions) overall, but it is ambiguous as it neglects information about the mass of the halos found. Here we proceed to explore this mass dependence.

In order to study the relationship between SBLAs and the masses of halos, we separated halos into mass bins of width $10^{0.4} M_{\odot}$, from $10^9 M_{\odot}$ to $10^{13} M_{\odot}$ at $z = 2$ and $10^{12.6} M_{\odot}$ at $z = 3$. We selected these mass intervals in order to obtain at least 15 halos per bin (see Table 1).

Table 1. Number of halos, n_h , per mass bin, for each redshift.

	$z = 2$	$z = 3$
Mass bin [$\log(M_h/M_{\odot})$]	n_h	n_h
[9, 9.4)	68 482	70 042
[9.4, 9.8)	29 382	29 485
[9.8, 10.2)	12 863	12 655
[10.2, 10.6)	5 562	5 260
[10.6, 11)	2 412	2 085
[11, 11.4)	1 043	775
[11.4, 11.8)	444	285
[11.8, 12.2)	172	85
[12.2, 12.6)	40	23
[12.6, 13)	17	4
> 13	4	0

We then found how many SBLAs are associated with halos in a given mass bin following the procedure set out in Sect. 3, and divided this number by the total number of SBLAs found, as per Eq. 4 – we called this new statistic $P(M_h)$.

Note that each mass bin probability is calculated independently of the others and that integrating $P(M_h)$ over the mass range to be studied does not yield P_{tot} , but an overestimation of it. SBLAs can be associated with more than one halo, with different masses, so they can be counted simultaneously in different mass bins. This arises not because our halos don't overlap physically, but due to halo and gas peculiar motions and the finger of God redshift smearing of both halo and SBLAs.

Fig. 3 shows $P(M_h)$ for our three standard flux limits and our two redshifts. It is immediately clear that SBLAs found in SDSS-like spectra at $z = 2$ broadly favour halo masses of around $10^{11.5} M_{\odot}$, irrespective of the flux limit. Similarly, $z = 3$ SBLAs favour halos with a mass of around $10^{11} M_{\odot}$. In other words, we find that $P(M_h)$ follows a distribution that has a peak probability (20% for $z = 2$ and 10% for $z = 3$) in the halo mass bin of $10^{11.4} M_{\odot} < M_h < 10^{11.8} M_{\odot}$ in all of the flux limits, for all redshifts.

To estimate the errors visible in Fig. 3, we performed a simple bootstrap analysis. Firstly, we resampled our SBLA samples 100 times. We then calculated $P(M_h)$ for each bootstrap realisation and estimated the uncertainty using the standard deviation of the distribution of calculated $P(M_h)$ values. This gives us the gray shaded areas present in the aforementioned figure. Overall, statistical errors are low, only becoming noticeable at $F_{\text{Ly}\alpha} < 0.05$ at $z = 2$, due to the low number of SBLAs present in this sample.

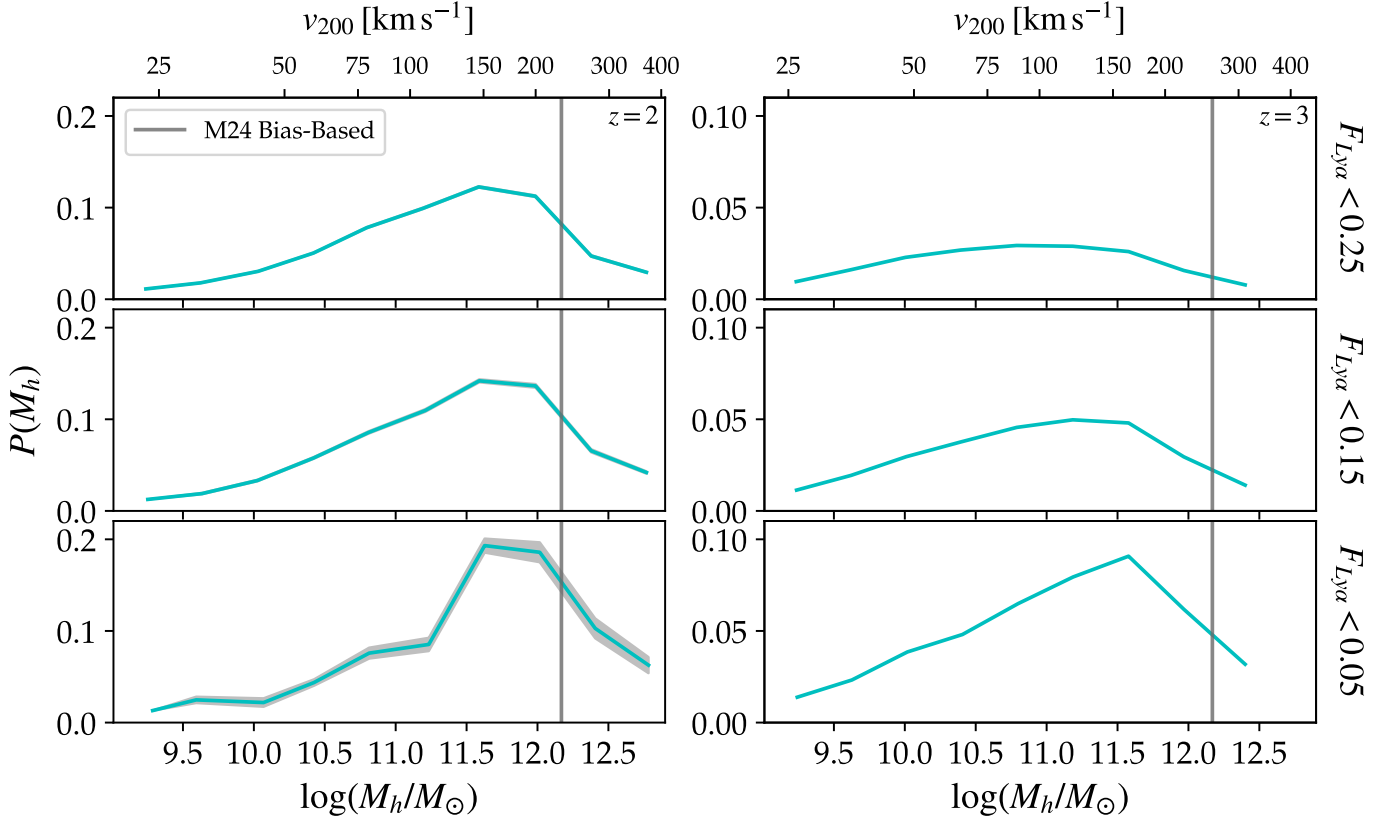


Fig. 3. $P(M_h)$ of the SDSS-like 2-pixel resolution ($v_{\text{SBLA}} = 138 \text{ km s}^{-1}$) spectra. $z = 2$ results are on the left panels and $z = 3$ results are on the right. The top axis represent the equivalent halo circular velocity for each halo mass, according to a linear fit we performed. The full vertical line represents the halo mass measurement from SBLA bias in M24. The grey shaded area represents the statistical errors estimated from the bootstrap analysis. Each row represents, from top to bottom, a different flux limit: $F_{\text{Ly}\alpha} < 0.25$, $F_{\text{Ly}\alpha} < 0.15$ and $F_{\text{Ly}\alpha} < 0.05$.

We can compare this favoured halo mass to the inferred halo mass from SDSS-IV/eBOSS DR16 data in M24 of $\approx 10^{12.17} M_{\odot}$, shown in Fig. 3 as the vertical grey line. To estimate this mass, they cross-correlated their more robust FS0 sample with the entire eBOSS DR16 Lyman- α forest sample, the amplitude of which provided an SBLA bias constraint of $b = 2.34 \pm 0.06$. Integrating a halo mass function, one can infer from this a halo mass, which is significantly higher than the majority of SBLAs studied in this simulation work. However, they must assume a halo mass function slope and a mass range over which to integrate. Perhaps, more importantly, the correlation function has an effective weighting, and so an effective bias. On the other hand, the mean halo mass for our samples will be dominated by the high mass end (note the logarithmic scale of our halo masses) and so these different effective averages both produce a higher mass than the one that can be inferred from Fig. 3. For $z = 2$ and the $F_{\text{Ly}\alpha} < 0.25$ case, we find that SDSS SBLAs trace a mean halo mass of $\approx 10^{12.25} M_{\odot}$, in excellent agreement with M24 estimate (a 20% difference).

The median halo mass is 0.7 – 1.4 dex lower (see red points in Fig. 9) offering a potential explanation for why bias-based estimates halo mass for SBLAs and DLAs (Pérez-Ràfols et al. 2018, 2023) are surprisingly high with respect to what one might expect (Bird et al. 2014); the bias measurements leads one to infer a mean halo mass while the typical halo masses are lower by around an order of magnitude. See Sect. 5.3 for a more extensive discussion of how SBLAs relate to halo mass.

There is a trend when we shift from $z = 2$ to $z = 3$ where the probability to find SBLAs inside halos diminishes, but this is expected. At $z = 3$ the mean opacity of the Lyman- α forest is higher, so there is a greater probability of finding strong, blended absorption in the IGM rather than the CGM – therefore it appears that the appropriate flux threshold to use must be optimised based on the needs of the study as a function of redshift.

Instead of looking at this from the point of view of the absorption systems, we can look at it from the point of view of the halos. In Eq. 5, we define a probe we call the ‘covering fraction’ (C_{frac}) in order to understand how SBLAs cover the projected areas of halos.

$$C_{\text{frac}} = \frac{\text{Numbers of lines-of-sight with SBLAs in a halo}}{\text{Total number of lines-of-sight in a halo}} \quad (5)$$

We recall that we remove the lines-of-sight with DLAs from the total number of lines-of-sight inside the halo. This is calculated for each individual halo, and we require the SBLAs to be associated with the halo in the redshift direction. The results can be seen in Fig. 4.

The differences between $z = 2$ and $z = 3$ are evident upon a first viewing. At $z = 2$, we can see that overall covering fractions are low for most halos, barely reaching 25% even for the inclusive flux limit of $F_{\text{Ly}\alpha} < 0.25$, compared with the higher values for $z = 3$, where even at the most restrictive flux limit ($F_{\text{Ly}\alpha} < 0.05$), we still reach higher values of the covering fraction than at $z = 2$. The conclusions from this are twofold: at

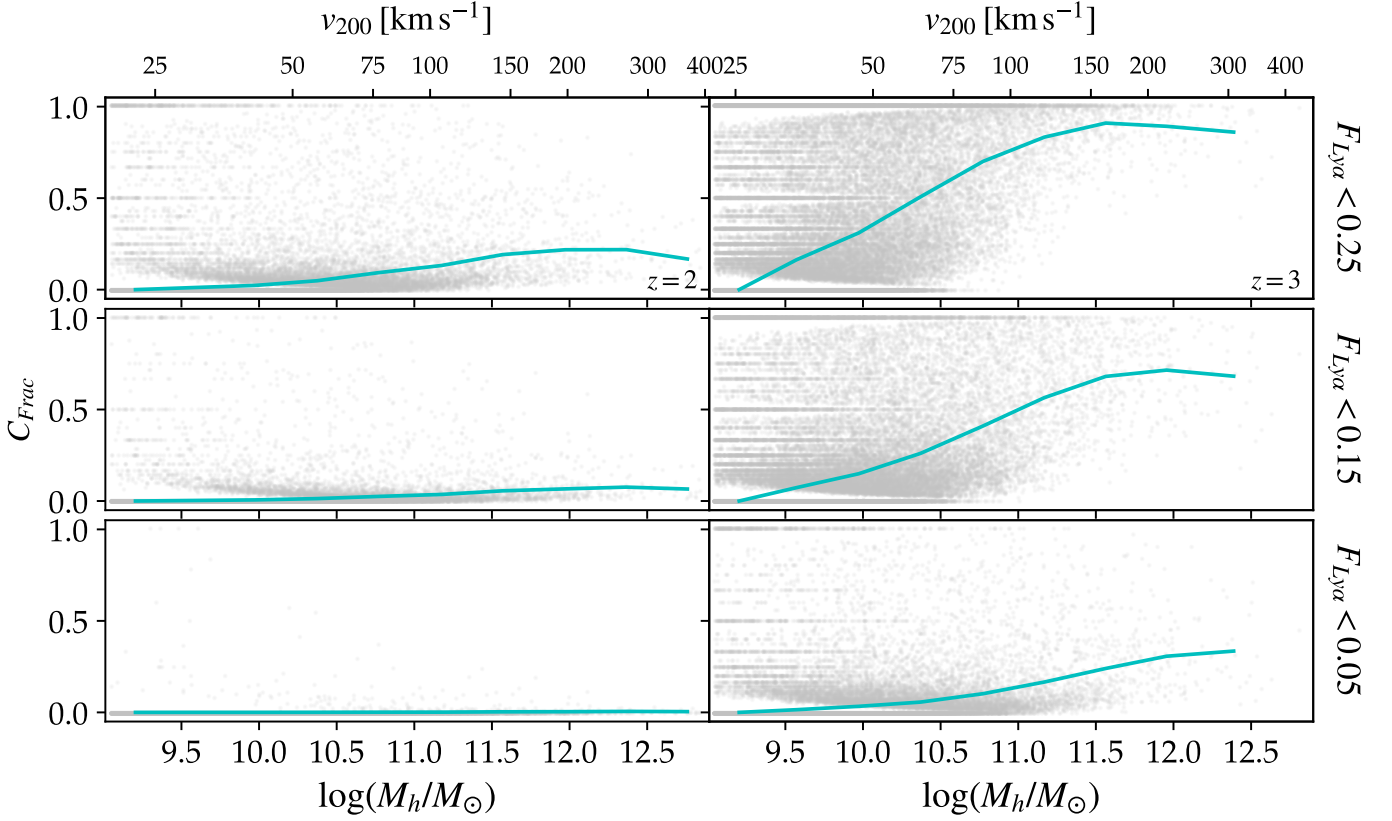


Fig. 4. Covering fraction of the SDSS-like 2-pixel resolution ($v_{\text{SBLA}} = 138 \text{ km s}^{-1}$) spectra, divided in mass bins. $z = 2$ results are on the left panels and $z = 3$ results are on the right. The grey points represent the covering fraction for each individual halo, while the solid cyan line represents the mean covering fraction for each mass bin mentioned in the text. All remaining elements are the same as in Fig. 3.

$z = 2$, the lower number of SBLAs gives us halos with less coverage, but with a high $P(M_h)$ – implying that, although they are not very common, they are still likely to be inside halos – and, at $z = 3$, although we have a higher number of halos with a significant fraction of SBLAs, there are still many present outside of them, no doubt due to the similarities in the states between the IGM and the CGM at this epoch.

However, we are considering only SBLAs with a specific spectral size. If we vary this property, what would they trace?

5. Variable SBLA Spectral Size

We have explored the relationship between standard SBLAs studied in the literature (P10; P14; M24) limited by SDSS resolution. We now broaden our analysis to explore the potential SBLA samples made possible without this restriction, and their relationship with dark matter halos. Much like the previous section, we also calculated the incidence rates for each SBLA spectral size and for each flux transmission limit, which is explained in Appendix A.

We are further motivated in this analysis by a striking hypothesis in M24: if the 138 km s^{-1} SBLA blend scale arises due to optically thin neutral hydrogen filling the light path through virialised halos with a velocity dispersion corresponding to the halo circular velocity, this would correspond to a halo mass of $\sim 10^{11.6} M_\odot$ (see Sect. 6.3 for a more in-depth discussion of this hypothesis). While this is lower than their inferred halo mass from clustering by around 0.5 dex, it is similar and offers the tantalising prospect that different blending-scales (or, different

spectral sizes) may allow one to identify different galaxy halos and their masses, and so study their CGM properties in absorption. We explore that potential in this section.

5.1. Total Probability for Varying SBLA Spectral Size

We rebinned the spectra on 15 distinct scales in the range $54 \text{ km s}^{-1} \leq v_{\text{SBLA}} \leq 483 \text{ km s}^{-1}$ in $\approx 30 \text{ km s}^{-1}$ increments to reflect 15 different SBLA widths for this study. The minimum corresponds to the typical full-width half-maximum of the spectral resolution in the blue portion of the low resolution mode of the WEAVE instrument (Dalton et al. 2012), and the WEAVE-QSO survey (Jin et al. 2024, Pieri et al. 2016, Pieri et al in prep). The maximum is selected to reflect the challenge of identifying sub-DLA damping wings in real data on $\approx 6 \text{ \AA}$ scales and to provide sufficient statistics in our synthetic spectra. We find between $10^3 - 10^7$ SBLAs at $z = 2$, and between $10^4 - 10^7$ at $z = 3$.

As we increase the spectral size of the SBLAs, we find that P_{tot} gradually increases, with values ranging between 18–68% at $z = 2$ and 5–36% at $z = 3$ (see Table A.3 for more details). The tendency we’ve seen with the SDSS-like SBLA spectral size of lower flux limits having higher probabilities still holds true here as well. These results remain consistent with the results of P14, although they are lower than the SDSS-like probabilities, even when we include the same size in our rebins (see Sect. 6.2 for an explanation as to why).

However, as mentioned previously, looking at P_{tot} gives us an incomplete picture of the kind of halos we trace, as these objects are more likely to trace halos of a specific mass range.

5.2. Halo Mass Dependence for Varying SBLA Spectral Size

Due to the limiting nature of P_{tot} , we once again calculated the $P(M_h)$ for each SBLA spectral size, in the same mass bins as mentioned for the SDSS 2-pixel case. An example of $z = 2$ and $F_{Ly\alpha} < 0.15$ can be seen in the top panel of Fig. 5 (for all cases, we refer readers to Appendix B).

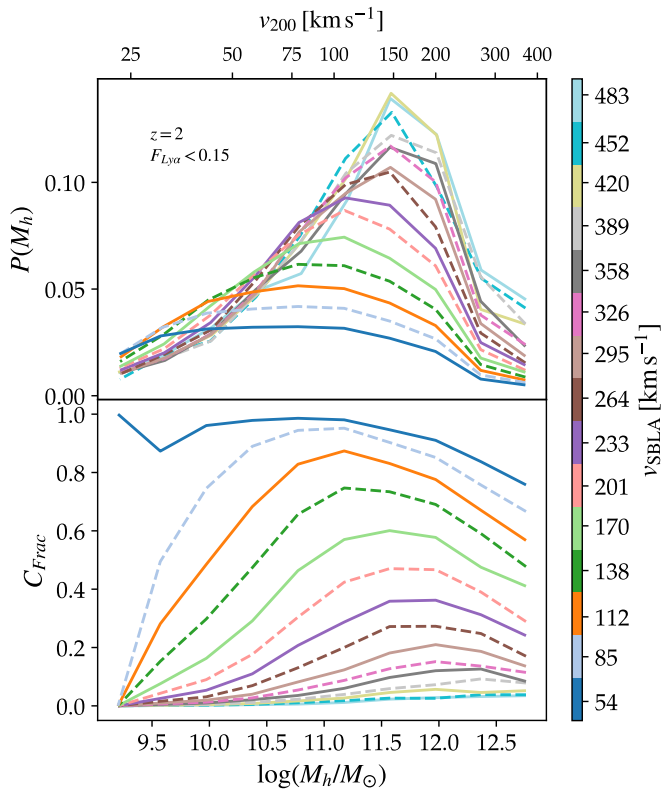


Fig. 5. $P(M_h)$ (top panel) and C_{Frac} (bottom panel), for the variable SBLA size. This is an example at $z = 2$ and $F_{Ly\alpha} < 0.15$. The colourbar on the side shows which line is which SBLA size. The full and dashed lines serve only as a visual aid.

At $z = 2$, we can see that, as we increase the spectral size of the SBLAs, we are more and more likely to find halos and, interestingly, the peak of the distribution becomes more pronounced and shifts towards higher halo masses. The fact that probabilities increase with the SBLA spectral size is likely because we detect less SBLAs overall, making $P(M_h)$ more pronounced. At $z = 3$, the $P(M_h)$ value is overall about half of the $z = 2$ values (which is expected), even if the overall pattern remains the same, so the same conclusions can be drawn: SBLAs of different spectral sizes appear to trace different halo masses.

But what about the halo-centric point of view? We once again calculate C_{Frac} , where we can see the $z = 2$ and $F_{Ly\alpha} < 0.15$ case in the bottom panel of Fig. 5 (for all cases, we refer readers to Appendix B). At $z = 2$, we can see that the smallest SBLAs ($< 112 \text{ km s}^{-1}$) cover a large fraction of halos of every mass and for every flux limit, but as we increase the size of the absorbers, we start to see that the covering fraction lowers significantly, with the larger SBLAs ($> 264 \text{ km s}^{-1}$) having no

presence in the lower mass halos. This naturally follows from $P(M_h)$ where, even though smaller SBLAs exist in abundance and are also covered by most lines-of-sights in halos, parsing which ones are influenced by halos and which ones are IGM is difficult, while larger SBLAs are rarer (although still abundant) and exist in fewer lines-of-sight, but are very likely to be associated with halos when found.

An important ambiguity of the results set out in this section arise due the self-evident fact that extended absorption seen in wide blends (characterised by high v_{SBLA}) will frequently be composed of smaller blends of strong absorption (i.e. low v_{SBLA}). Small SBLAs are numerous, partly because strong absorption over a narrower velocity window is more common (while larger binning naturally draws the forest transmission to the mean). Small SBLAs are also numerous because several can exist within a single larger SBLA. In other words, a particular blending scale thus far (including the work of P10, P14 and M24) effectively defines a minimum SBLA width that includes higher v_{SBLA} absorption systems. In the next section we aim to address this ambiguity and assign SBLAs a correct and unique v_{SBLA} , and in doing so improve both their veracity and utility.

5.3. Hierarchical Framework

In the previous section, we found that SBLAs seem to associate with halos in a manner such that the halo masses are sensitive to spectral size, but this neglects the fact that extended absorbing structures are made of potentially numerous smaller ones. In many cases smaller SBLAs must be sub-divisions of larger SBLAs. How do we address this? We simply assume that the largest SBLA trace the structure and the smaller SBLAs within them add duplication with less physical value.

In effect, we have thus far treated the Lyman- α forest as an analogue for a Gaussian linear density field in Press–Schechter formalism (Press & Schechter 1974). Strong absorption on a given scale equates to overdensity on a given smoothing scale. A large-scale ‘absorption overdensity’ beyond a critical overdensity, like the linear density field, is approximated as collapsed. The smoothing scale corresponds to a characteristic pre-collapse scale, which in turn corresponds to a halo mass. A limitation of this formalism is that it doesn’t naturally account for halo mergers – halo incidence is considered independently of whether they reside in larger structures that collapse around them. The same limitation affects the SBLA decomposition presented thus far. We can address this using the same simple method applied in Scannapieco & Broadhurst (2001) and Pieri et al. (2007), namely that lower mass halos within a higher mass halo are considered to have merged to form the larger halo. Likewise, here smaller SBLAs that reside within a larger SBLA are consider to have merged to form the larger halo. In effect, we build a hierarchical merger tree analogue. Note that no reference to substructure is intended here, since these smaller halos are treated as ‘absorbed’ and to treat them as persisting as a substructure is likely to be an over-interpretation of the analogy and the simple framework used.

We proceed by requiring that larger SBLAs consume the smaller ones (for each redshift and flux limit), until only the independent ones remain. Therefore the hierarchical SBLA samples will more closely reflect the natural extent of their absorption complex. To do this, we go spectrum by spectrum, starting with the largest SBLAs and searching for those smaller SBLAs centred within their boundaries, in which case they are considered ‘consumed’ and are removed from our list. We proceed down the SBLA hierarchy allowing surviving SBLAs on each

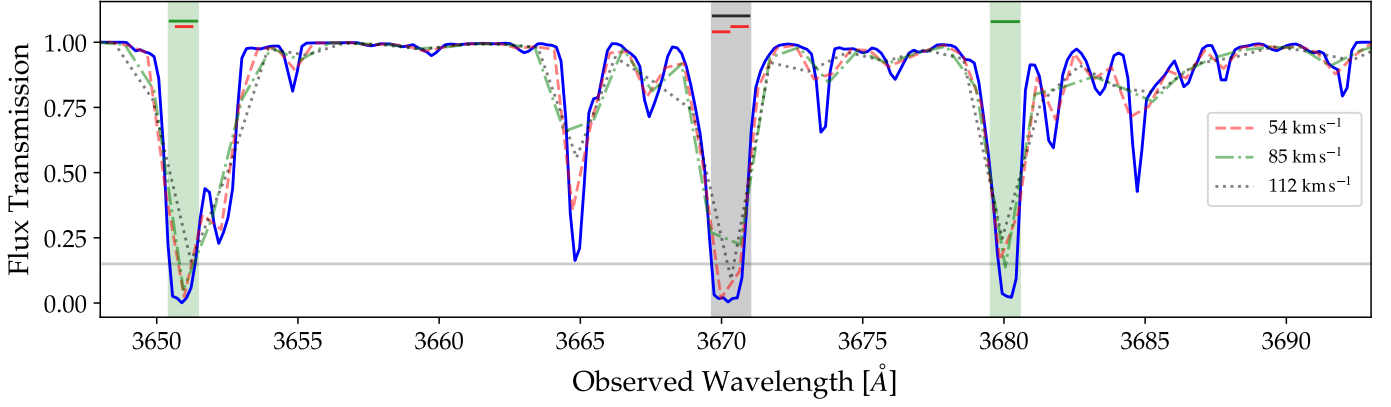


Fig. 6. Example of how the hierarchy of SBLAs works. This is an example at $z = 2$ and $F_{Ly\alpha} < 0.15$. The horizontal gray line represents when $F_{Ly\alpha} = 0.15$. The blue full line represents the spectrum in its full resolution. The red dashed, green dot-dashed and black dotted lines represent the spectrum rebinned to 54, 85 and 112 km s^{-1} , respectively. The red, green and black horizontal bars represent the spectral size of SBLAs with $v_{\text{SBLA}} = 54, 85$ and 112 km s^{-1} , respectively. The vertical coloured bars represent the size of the independent SBLAs. On the left, we can see that the SBLA with 85 km s^{-1} fits one SBLA with 54 km s^{-1} inside the same absorption feature, while on the middle the SBLA with 112 km s^{-1} can fit two SBLAs with 54 km s^{-1} .

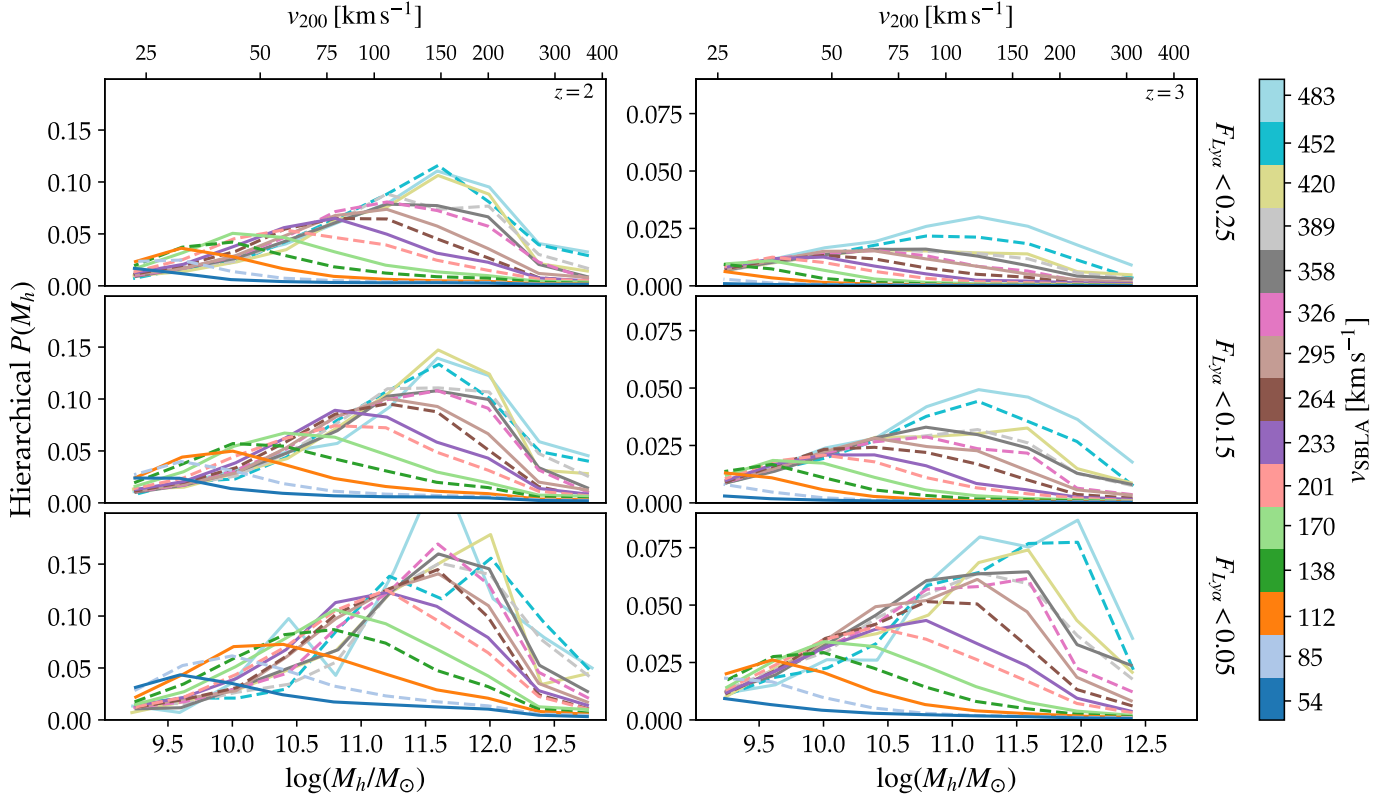


Fig. 7. Hierarchical $P(M_h)$. $z = 2$ results are on the left panels and $z = 3$ results are on the right. Flux limits decrease from top to bottom. The colourbar on the side shows which line is which SBLA size. The full and dashed lines serve only as a visual aid.

size tier to consume smaller SBLAs centered within their boundaries as we go. See Fig. 6 for an example of this in action.

In Fig. 7, we reconstructed a new $P(M_h)$ statistic from this hierarchical list of absorbers, in order to understand the performance of the new halo mass estimation scheme. We also estimated a new total probability, $P_{h,tot}$, which is similar to P_{tot} at the larger SBLA end, while at the smaller absorber end (below 170 km s^{-1}) they suffer from a drop, due to the fact that many of

them were consumed by their larger counterparts, and the ones that remain lie mostly outside halos (see Table A.3 for more details).

The C_{Frac} of the hierarchical SBLAs can be found in Fig. 8. We opted for a cumulative approach, where each line represents the covering fraction of an SBLA spectral size and all of the ones larger than it, i.e., C_{Frac} of $v_{\text{SBLA}} = 85 \text{ km s}^{-1}$ includes all SBLA spectral sizes up until 483 km s^{-1} , but excludes

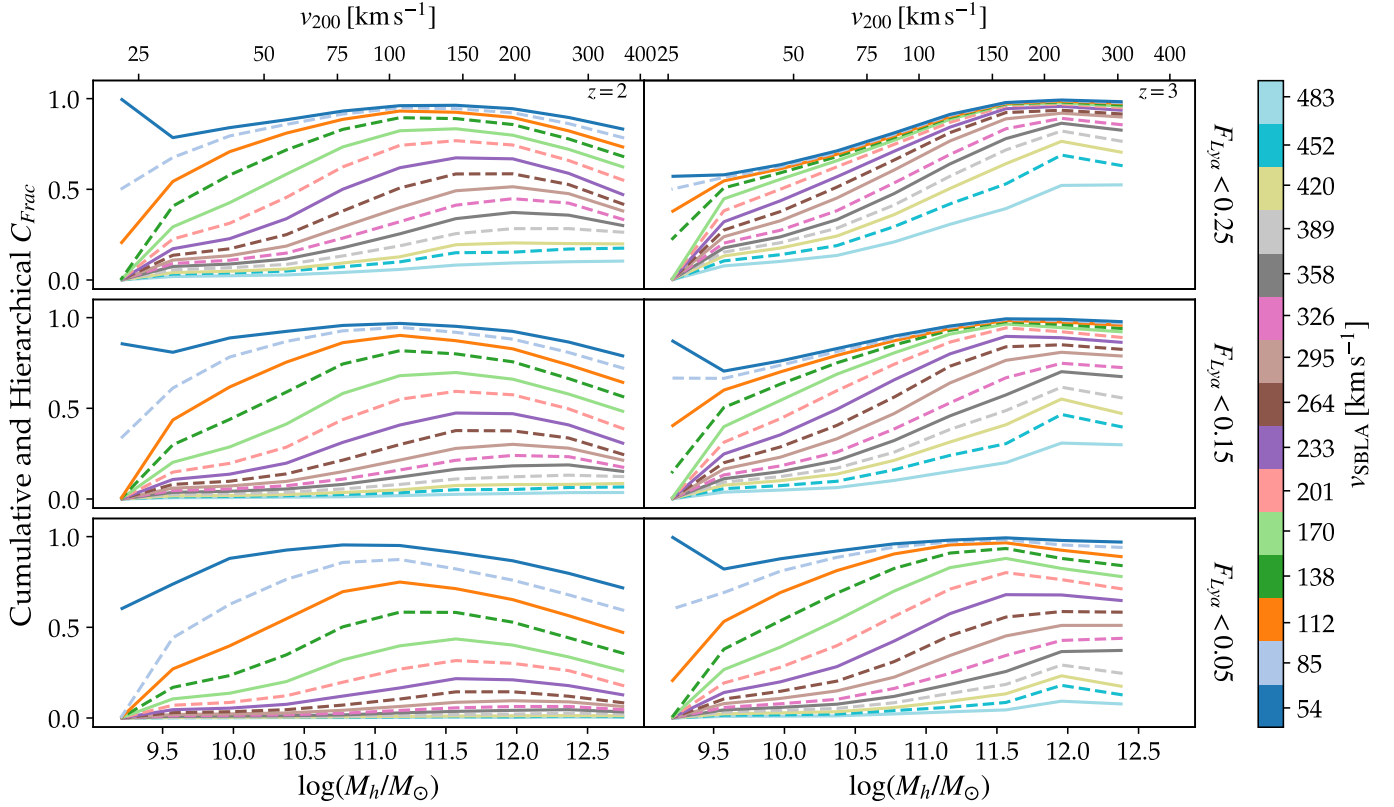


Fig. 8. Covering fraction of SBLAs in the hierarchical framework, divided in mass bins. $z = 2$ results are on the left panels and $z = 3$ results are on the right. The colourbar on the side shows which line is which cumulative v_{SBLA} size: the full dark blue line represents C_{Frac} of the 54 km s^{-1} SBLA and all the above, the dashed light blue represents the C_{Frac} of the 85 km s^{-1} SBLA and all the above, and so on until we only have the 483 km s^{-1} SBLA size. All remaining elements are the same as in Fig. 7. The full and dashed lines serve only as a visual aid.

$v_{\text{SBLA}} = 54 \text{ km s}^{-1}$. This was chosen because looking at one specific SBLA spectral size in the covering fraction does not follow the same principle in the hierarchical and non-hierarchical frameworks, as many SBLAs have been consumed by their larger counterparts. In any case, the same patterns that were seen in the non-hierarchical case are still prevalent here, where larger SBLAs are still rarer than smaller ones, but the combination of all the SBLAs together (see the dark blue line in all plots) shows a very optimistic scenario of the detection of SBLAs in halos, as even when many of the smaller SBLAs are consumed by the larger ones, we still find very high values of C_{Frac} .

This statistic tells us about the halo finding purity of the complete suite of SBLAs (or how effectively SBLAs find halos according to each criterion). There’s a clear dependence with the flux limit and the size of the SBLA, with the cost that as we increase the purity of the sample, the covering fraction decreases.

The hierarchical framework shows a clear distinction from the previous $P(M_h)$ estimations (see top panel of Fig. 5). We can see that for most SBLA spectral sizes, instead of having a broad distribution, it becomes more peaked for all but the largest SBLA sample (which, by definition, is unaffected by the hierarchical framework). Smaller SBLAs ($< 170 \text{ km s}^{-1}$) probe high mass halos less often in the hierarchical framework, since the larger SBLAs tend to find these halos and suppress duplication from smaller SBLAs. This tells us that, with this hierarchical framework, these smaller SBLAs are much more likely to trace halos of a specific mass range (depending on the size of the absorber) than in a non-hierarchical framework. This ‘peakiness’ of the

distributions applies to the larger SBLAs as well, although with less of an impact as in the smaller ones.

There is a clear correlation between halo mass and SBLA size, implying that we can find halos of a specific mass depending on which spectral binning we consider. Analysing the placement and associated absorption with this suite of SBLAs will allow us to probe different halo masses and the different properties of the CGM of their associated galaxies.

In order to understand what is the typical halo mass associated with an SBLA, we calculated both the mean and the median mass of each SBLA spectral size, whose results can be seen in Fig. 9. It is important to note that, when calculating this, we considered only masses below $10^{13} M_{\odot}$ for $z = 2$ and below $10^{12.6} M_{\odot}$ for $z = 3$, given the limited statistics for larger SBLAs. We can see that the overall trend of increasing the mass as we increase the spectral size of the absorbers is present in most flux limits for both redshifts. Relevant to note here is that, when compared to the non-hierarchical case (see the blue dotted line), the relationship between median halo mass and v_{SBLA} in the hierarchical SBLAs possesses a range of masses that is wider (nearly 2 dex) than its non-hierarchical counterpart (about 0.9 dex), further reinforcing the fact that with this framework we are able to better understand what halo mass each SBLA spectral size is likely to trace.

The only exception to these observations appear to be the $v_{\text{SBLA}} < 85 \text{ km s}^{-1}$ regime (without Gaussian smoothing) at $z = 3$ where the scatter is simultaneously large and the overall probabilities of halo finding are low. It appears that the ca-

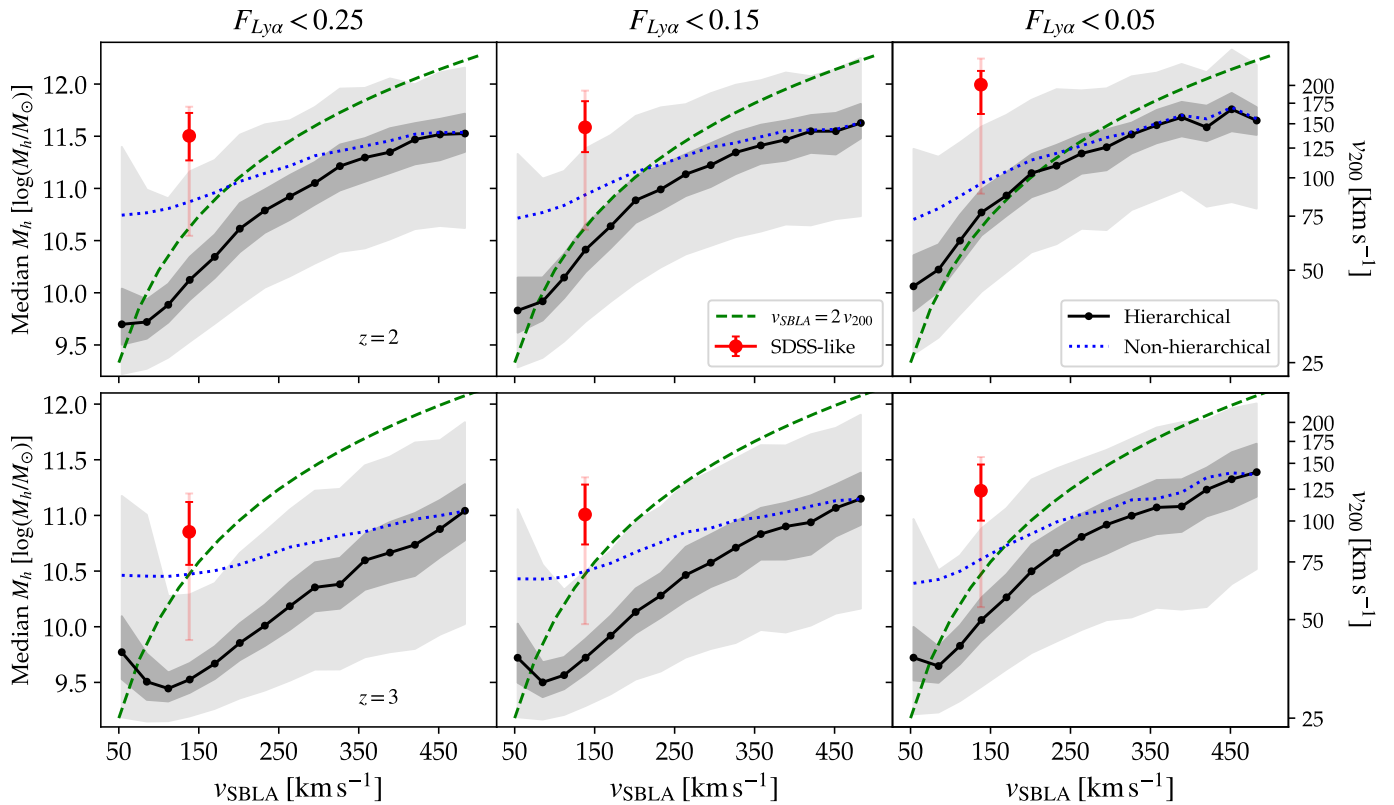


Fig. 9. Median halo masses associated with SBLAs of varying size. $z = 2$ results are shown in the top panels and $z = 3$ on the bottom. Flux limits are reduced progressively in panels from left to right. The black line shows the median halo mass for each SBLA size in the hierarchical framework with the dark (light) grey shaded area representing the 0.5σ (1σ) spread. The dotted blue line represents the median of the non-hierarchical sample. The red points represent the SDSS sized SBLAs, with the dark (light) red error bar representing the 0.5σ (1σ). The green dashed line represents the $v_{\text{SBLA}} = 2 v_{200}$ hypothesis (see Sect. 6.3).

capacity of SBLAs in finding halos breaks down for the smallest SBLAs, particularly at $z = 3$ where contamination is more common. The failure is remediated somewhat by limiting oneself to the strongest absorption possible ($F_{\text{Ly}\alpha} < 0.05$).

6. Discussion

The exploration of strong-blended Lyman- α systems in P10, P14 and M24 demonstrated that SBLAs offer an expanded set of halos in absorption that can be used to find and study the circumgalactic medium. In this work, we examined the halo finding probability and completeness, the halo covering fraction and the typical halo mass traced by SBLAs using the TNG50 simulation. We further generalised the definition of SBLAs and took the first steps towards optimising the finding of halos. We introduce the ‘SBLA hierarchical framework’ to the community as a powerful tool for decomposing Lyman- α spectra into a series of halos surrounded by IGM absorption.

In order to further examine the relationship between SBLAs and halos, in this section we look at many pertinent topics left to address: uncertainties arising from our use of hydrodynamic simulations; the effects of smoothing in the spectra; the relationship between SBLA spectral size, halo mass, and halo circular velocity; how to choose a sample to study the CGM or the IGM; and our definition of the boundary of the CGM.

6.1. Hydrodynamic Simulation Limitations

Although the TNG50 simulation possesses exquisite resolution and is able to provide us with many details about the Universe, there are still some caveats we must address with our results. The first one is that the TNG50 simulation does not resolve the parsec-scale clumping associated with SBLAs as inferred in P10, P14 and M24. The second is that we have rescaled the optical depth of the spectra at each redshift in order to ensure that the mean optical depth follows the measurements of Faucher-Giguère et al. (2008).

These two factors imply that the synthetic spectra that we used to select SBLAs may not be perfectly representative of observations. Any such small-scale structure would impact metal absorption properties, and may also have an impact on associated Lyman- α absorption. Meanwhile a global mean opacity consistent with observations does not guarantee obtaining the correct representation for the $\approx 1\%$ of the forest associated with CGM absorbers. Both these subtleties may have an impact on our results.

Comparing incidence rates, dn/dz , with values from observations, gives us a window into how this may affect the SBLA estimates (see Appendix A for more details). We find that there seems to be a discrepancy of up to two orders of magnitude between incidence rates from our SDSS-like spectra and the smoothed and rebinned KODIAQ and SQUAD spectra (so that they resemble SDSS). We find this result at both redshifts, though dampened at $z = 3$, perhaps implying that this may in-

dicating tensions with the TNG50 simulation results, its physical model, our treatment of the UV Background and neutral hydrogen modelling, and/or our synthetic spectra post-processing.

Even with this in mind, this does not detract from the fact that we are still able to replicate results from M24, namely the halo mass estimate from the SDSS-like spectra.

6.2. Smoothing Effects

We have thus far treated the SBLA spectral size derived from the resolved spectra as a variable that can be applied to any case, i.e. any resolution or instrument. However, when we compare Fig. 3 with Fig. 5, we can see that this is not the case: the SDSS-like SBLAs, although technically possessing a $v_{\text{SBLA}} = 138 \text{ km s}^{-1}$, do not behave in the same way as the resolved SBLAs of the same size. The reason for this traces back to the fact that the SDSS spectra are smoothed by instrumental broadening on a scale that exceeds the wavelength resolution, with the full width at half-maximum (FWHM) varying between $138 - 179 \text{ km s}^{-1}$ (P14), changing the effective spectral size of the SBLAs that we trace.

In order to compare how the smoothing affects the estimates from SBLAs, we can look at the median halo mass estimates from the resolved SBLAs and the SDSS-like SBLAs, visible in the black line and red dot in Fig. 9, respectively. The differences between the v_{SBLA} in SDSS and the resolved spectra become clear here as, for the same size, two clearly distinct halo masses are preferred, with almost no overlap in the spread. Effectively, this means that the SDSS-like SBLAs are comparable with the resolved SBLAs that have $v_{\text{SBLA}} > 400 \text{ km s}^{-1}$. As such, a connection between these two cases should then be made with these spectral sizes, and not with a direct one-to-one relation.

Exploring the effects of smoothing in SBLA detection and halo tracing is outside of the scope of this work, but it is something that will be explored in future work, both with real high-resolution data, as well as a continuation of this simulation work.

6.3. A Toy Model for SBLA Spectral Size, Halo Mass and Halo Circular Velocity

In addition to the inferred mean halo mass derived from a forest cross-correlation (as discussed in Sect. 4.2), M24 put forward a hypothesis as to why SBLAs are associated with halos. The picture proposed is one where halos are filled with optically thin gas clouds (or some smoothly varying gas distribution equivalent) that trace the dark matter dynamics. In fact, if we look at the distribution of line-of-sight velocities of halos (e.g. Fig. 3 of Weng et al. 2024), we can see that even in evolved systems we have components that possess the same velocity as the halo circular velocity – equivalent to our v_{200} . This directly implies that SBLAs of different sizes could be tracing different halo masses, which is the M24 hypothesis.

The median halo mass associated with the hierarchical SBLA sample bears this out in qualitative terms (see Fig. 9), but we may assess the prediction quantitatively. Furthermore, we may also reflect on the accuracy of the hypothesis in light of our analysis, and consider what this tells us about why SBLAs are such an effective halo finding machine.

We require SBLAs to be associated with halos if they are inside the viral radius (see Eq. 2) and within $2 v_{200}$ in velocity space (see Eq. 3). This requirement does not necessarily mean that v_{SBLA} will equal twice v_{200} , but it is a reasonable expectation value based on this hypothesis. Note that we use hard limits

on the decision of halo in/out and SBLA boundaries here, but halos are not hard edged (see Sect. 6.5) and in SDSS the Gaussian instrumental broadening clearly plays a role (as explained in Sect. 6.2).

Turning back again to Fig. 9, we compare the median halo mass estimate, in the black line, with the hypothesised value of $v_{\text{SBLA}} = 2 v_{200}$, in the green dashed line. At $z = 2$, we can see that, as we lower the flux limit, our estimates increasingly align with this hypothesis, with failure to conform to this expectation coming from the smallest SBLAs ($v_{\text{SBLA}} \leq 85 \text{ km s}^{-1}$). In any case, most SBLA sizes reside below this line, implying that this hypothesis is a good indicator of the upper limit of the halo mass that SBLAs trace. For $z = 3$, this is also true, with the caveat that once again the smallest SBLAs do not conform to the expectation of the hypothesis.

The SDSS-like SBLAs at $z = 3$ seem to match the v_{200} directly, with no need for the adjustment to the $2 v_{200}$, no doubt due to the smoothing kernel. At $z = 2$, we typically get higher v_{SBLA} than v_{200} , but it is less than the aforementioned $v_{\text{SBLA}} = 2 v_{200}$.

6.4. CGM and IGM Sample Selection

With the hierarchical framework, we found that there is a striking relationship between SBLA size and typical halo mass traced, something that is not as evident in the non-hierarchical case. With this link established, the next step is to understand which sample of SBLAs we should use to study the CGM regions associated with these halos.

Of course one would like to build a CGM sample with an acceptable level of both purity and completeness, and the details of how one does this depends on both what is possible and the specific requirements of the study. In the previous section, we found that there is some small SBLA limit for which the probability that an SBLA finds a halo is rather low (see Fig. 7). Hence, it is natural to build a hierarchical SBLA sample down to some minimum v_{SBLA} to study a range of halo masses down to some chosen failure threshold. We therefore study purity and completeness as top-down cumulative statistics. Specifically the cumulative purity is the probability of finding any SBLA above a certain size, and the probability in question for any v_{SBLA} is $P_{h,tot}$.

We note that the purity here is distinct from the purity stated in M24. In M24, the purity was defined as the success of SBLA finding in light of observing noise. Here, purity is the success of halo finding from a set of SBLAs. Of course, the purity of halo finding from real observed absorption spectra is a combination of both these terms. This is further complicated by the fact that observed strong absorption often (given the skew transmission distribution) corresponds to a higher true flux transmission (see Fig. 3 of P14). This is in part why we explore the halo purity derived from varying flux limits – often an observed sample of SBLAs will correspond to a range of true fluxes, and we provide the reader with the halo purity across this useful flux range. Simply put, introducing noise to our spectra would result in less defined separations between samples with different flux limits.

Regarding completeness, we assess all lines-of-sight in halos with SBLAs of a certain size and above (a cumulative SBLA size, much like the purity) and divided them with all lines-of-sight in halos. For these estimates, we once again restricted the halo masses to the range defined in Sect. 4.2, where at $z = 2$ we consider $M_h < 10^{13} M_\odot$ and at $z = 3$ we consider $M_h < 10^{12.6} M_\odot$. This is similar to the covering fraction, but instead of having a mean per halo, we consider it a global statistic describing all lines-of-sight.

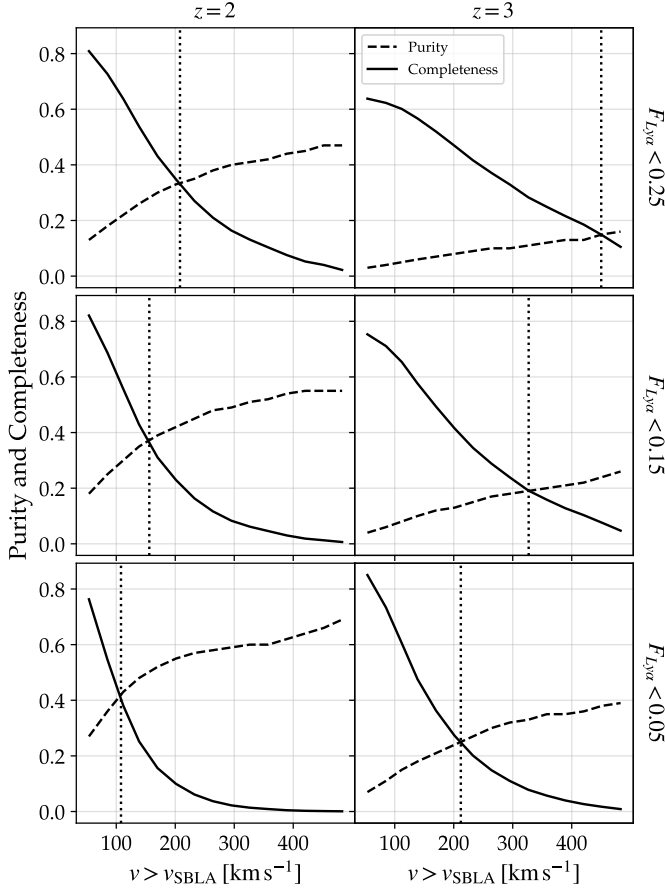


Fig. 10. Purity (or the cumulative $P_{h,tot}$, dashed line) and completeness (full line). The dotted vertical line represents the point where purity and completeness intersect. On the left hand panels, we have $z = 2$, and on the right we have $z = 3$, with the flux transmission limits decreasing from top to bottom.

The cumulative purity and completeness are shown in Fig. 10. In order to construct a sample of CGM systems to study, a good rule of thumb is to balance purity and completeness by looking for the point of equality. This provides us with a full SBLA sample based on a hierarchy with some minimum v_{SBLA} for any given flux limit. The preferred flux limit to select is $F_{Ly\alpha} < 0.05$ given that this provides the highest purity and completeness equality. In effect, at $z = 2$ we suggest an SBLA selection with $F_{Ly\alpha} < 0.05$ and $v_{SBLA} \geq 112 \text{ km s}^{-1}$, while at $z = 3$ we suggest $F_{Ly\alpha} < 0.05$ and $v_{SBLA} \geq 201 \text{ km s}^{-1}$.

These low flux transmissions require high signal-to-noise data (in light of SBLA purity analysis of M24). Probing halos of mass of $\approx 10^{10} M_{\odot}$ at $z = 2$ therefore require both high resolution spectra (to resolve $v_{SBLA} = 100 \text{ km s}^{-1}$) and high signal-to-noise (to reliably recover truth transmission of 5%).

One may wish to prioritise a complete sample of CGM systems with less priority on purity in order to trace baryon acoustic oscillations with the largest available sample of halos as was explored in Pérez-Rafols et al. (2023). On the other hand, one may wish to study a pure sample of IGM by excluding a more complete sample of CGM systems. For example, Morrison et al. (2021) used metal stacks to study the UV background spatial variation, with the including and exclusion of SBLAs. For such samples, we can choose to trade off some of the purity in the selection with a boost in completeness, by increasing the flux

limits and maintaining the v_{SBLA} for the CGM sample. Higher flux limits provide a larger number of SBLAs (see Table A.2), and allow to take into account the effects of noise (as explained when we compare our purity with the M24).

As such, for IGM studies, or completeness prioritised CGM samples, at $z = 2$ we suggest an SBLA sample with $F_{Ly\alpha} < 0.25$ and $v_{SBLA} \geq 112 \text{ km s}^{-1}$. At $z = 3$ suggestions for a large SBLA sample becomes more complicated, as at $F_{Ly\alpha} < 0.25$ we have low purity and completeness at nearly all v_{SBLA} . At $F_{Ly\alpha} < 0.15$ we have better values, so we suggest this flux limit as well as the previous SBLA size: $v_{SBLA} \geq 201 \text{ km s}^{-1}$.

6.5. Boundaries of the CGM Region

When we define the CGM in this work, we are assuming that the virial radius – which we define as the region of space where the density is 200 times the mean density of the Universe (Gunn & Gott 1972) – encompasses all (or most) of the particles that are tied to the central galaxy in the halo. However, this has been shown to not always be the case (e.g. Diemer et al. 2017; García et al. 2023).

If we consider one of these halo boundaries to replace the virial radius, we will expand the region of physical space which will, in turn, affect our statistics. The P_{tot} and $P(M_h)$ statistics (hierarchical or not) will increase, as more SBLAs will be included inside the CGM regions of galaxies. When it comes to C_{Frac} , the impact is more subtle, as it depends on the gas properties of the increased radius for each halo.

This is only considering extensions to the CGM definition in physical space, but the truth is that velocity space would be affected as well: v_{200} could be an insufficient measurement to describe where SBLAs reside spectroscopically in the halos. However, there does not seem to exist a relationship between increasing the radius of a halo and increasing/decreasing the spectral velocity of the components present in it (see Fig. 9 of Weng et al. 2024), so while changing the radius of the halo is expected to have an impact in the physical space, in velocity space our results should remain unchanged.

7. Conclusions

Strong, Blended Lyman- α (SBLA) absorbers have already been shown to have the potential to detect many halos in the Lyman- α Forest (P10; P14; M24). With this work, we study this observational phenomenon and explore which halos are traced by SBLAs. We do this by exploiting absorption spectra generated from the TNG50 cosmological hydrodynamical simulation. We possess 4 million parallel lines-of-sight, randomly spread throughout the box, with minimum wavelength of 3645 Å (4870 Å) and a maximum wavelength of 3695 Å (4930 Å), at $z = 2$ ($z = 3$). We study have these spectra in two resolutions: SDSS-like ($\Delta v = 69 \text{ km s}^{-1}$) and ‘resolved’ (4.5 km s^{-1}).

We find that:

- In SDSS resolution, SBLAs with the lower Lyman- α flux transmission ($F_{Ly\alpha} < 0.05$) have a 78% (42%) probability of finding halos at $z = 2$ ($z = 3$). A 10-15% drop in probability occurs per 10% increase in transmission to $F_{Ly\alpha} < 0.25$;
- The mean halo mass of these SDSS-like SBLAs is $10^{12.25} M_{\odot}$. This is consistent with the value derived in M24 based on clustering bias ($10^{12.17} M_{\odot}$) within their modelling uncertainty;
- SBLAs are more numerous and cover more halo lines-of-sight at higher redshifts and higher flux transmissions;

- In resolved spectra we are free to select the SBLA spectral size and do so between $54 \text{ km s}^{-1} \leq v_{\text{SBLA}} \leq 483 \text{ km s}^{-1}$. Upon doing so we find that the probability of finding halos increases with SBLA size and reduced flux transmission;
- We apply a hierarchical framework, allowing larger SBLAs to consume the smaller ones (see illustration in Fig. 6). This allows SBLAs to reach their natural spectral size and avoids duplication. With this refinement the halo mass distribution for a given SBLA spectral size becomes narrower with respect to the non-hierarchical case;
- In the hierarchical framework, we trace median halo masses from $M_h \approx 10^{9.5} M_\odot$ (for 100 km s^{-1} SBLAs) to $M_h \approx 10^{11.5} M_\odot$ (for 450 km s^{-1} SBLAs);
- In order to study the CGM, we recommend selecting SBLAs with the lower flux limit ($F_{\text{Ly}\alpha} < 0.05$) and with $v_{\text{SBLA}} \geq 112 \text{ km s}^{-1}$ ($v_{\text{SBLA}} \geq 201 \text{ km s}^{-1}$) for $z = 2$ ($z = 3$). For IGM studies, we suggest selecting SBLAs with $F_{\text{Ly}\alpha} < 0.25$ ($F_{\text{Ly}\alpha} < 0.15$) and $v_{\text{SBLA}} \geq 112 \text{ km s}^{-1}$ ($v_{\text{SBLA}} \geq 201 \text{ km s}^{-1}$) for $z = 2$ ($z = 3$).

In the future, we plan on applying this hierarchical framework to both high resolution data, such as KODIAQ (O’Meara et al. 2021), as well as lower resolution data, such as DESI (Levi et al. 2019; DESI Collaboration et al. 2024) or WEAVE-QSO (Pieri et al. 2016), as part of WEAVE (Dalton et al. 2012; Jin et al. 2024) to understand if the results from this work hold true. We also plan on exploring the effects of different rebin starting points in the SBLA selection, as well as different smoothing kernels. In terms of the simulated spectra, we want to make our analysis more sophisticated, by using machine learning methods.

Acknowledgements. This work was supported by the French National Research Agency (ANR) under contract ANR-22-CE31-0026 and by Programme National Cosmology et Galaxies (PNCG) of CNRS/INSU with INP and IN2P3, co-funded by CEA and CNES. D.N. acknowledges funding from the Deutsche Forschungsgemeinschaft (DFG) through an Emmy Noether Research Group (grant number NE 2441/1-1), and under Germany’s Excellence Strategy EXC 2181/1 - 390900948 (the Heidelberg STRUCTURES Excellence Cluster). This work made use of Astropy:³ a community-developed core Python package and an ecosystem of tools and resources for astronomy (Astropy Collaboration et al. 2013, 2018, 2022).

References

Astropy Collaboration, Price-Whelan, A. M., Lim, P. L., et al. 2022, *ApJ*, 935, 167
 Astropy Collaboration, Price-Whelan, A. M., Sipőcz, B. M., et al. 2018, *AJ*, 156, 123
 Astropy Collaboration, Robitaille, T. P., Tollerud, E. J., et al. 2013, *A&A*, 558, A33
 Bahcall, J. N. & Spitzer, Jr., L. 1969, *ApJ*, 156, L63
 Barcons, X., Lanzetta, K. M., & Webb, J. K. 1995, *Nature*, 376, 321
 Bergeron, J. & Stasińska, G. 1986, *A&A*, 169, 1
 Bird, S., Vogelsberger, M., Haehnelt, M., et al. 2014, *MNRAS*, 445, 2313
 Blitz, L. & Rosolowsky, E. 2006, *ApJ*, 650, 933
 Cai, Z., Fan, X., Bian, F., et al. 2017, *ApJ*, 839, 131
 Cai, Z., Fan, X., Peirani, S., et al. 2016, *ApJ*, 833, 135
 Chen, H.-W., Kennicutt, Jr., R. C., & Rauch, M. 2005, *ApJ*, 620, 703
 Chen, H.-W., Lanzetta, K. M., Webb, J. K., & Barcons, X. 1998, *ApJ*, 498, 77
 Croft, R. A. C., Weinberg, D. H., Katz, N., & Hernquist, L. 1998, *ApJ*, 495, 44
 Dalton, G., Trager, S. C., Abrams, D. C., et al. 2012, in *Society of Photo-Optical Instrumentation Engineers (SPIE) Conference Series*, Vol. 8446, Ground-based and Airborne Instrumentation for Astronomy IV, ed. I. S. McLean, S. K. Ramsay, & H. Takami, 84460P
 Dekel, A. & Mandelker, N. 2014, *MNRAS*, 444, 2071
 DESI Collaboration, Adame, A. G., Aguilar, J., et al. 2024, *AJ*, 168, 58
 Diemer, B., Mansfield, P., Kravtsov, A. V., & More, S. 2017, *ApJ*, 843, 140

Faucher-Giguère, C.-A., Lidz, A., Zaldarriaga, M., & Hernquist, L. 2009, *ApJ*, 703, 1416
 Faucher-Giguère, C.-A., Prochaska, J. X., Lidz, A., Hernquist, L., & Zaldarriaga, M. 2008, *ApJ*, 681, 831
 Fukugita, M., Ichikawa, T., Gunn, J. E., et al. 1996, *AJ*, 111, 1748
 Fumagalli, M., O’Meara, J. M., Prochaska, J. X., & Worseck, G. 2013, *ApJ*, 775, 78
 García, R., Salazar, E., Rozo, E., et al. 2023, *MNRAS*, 521, 2464
 Genel, S., Vogelsberger, M., Springel, V., et al. 2014, *MNRAS*, 445, 175
 Gunn, J. E., Carr, M., Rockosi, C., et al. 1998, *AJ*, 116, 3040
 Gunn, J. E. & Gott, III, J. R. 1972, *ApJ*, 176, 1
 Gunn, J. E. & Peterson, B. A. 1965, *ApJ*, 142, 1633
 Heckman, T. M., Alexandroff, R. M., Borthakur, S., Overzier, R., & Leitherer, C. 2015, *ApJ*, 809, 147
 Henry, A., Scarlata, C., Martin, C. L., & Erb, D. 2015, *ApJ*, 809, 19
 Hoskin, M. A. 1976, *Journal for the History of Astronomy*, 7, 169
 Hu, T., Khaire, V., Hennawi, J. F., et al. 2025, *MNRAS*, 536, 1
 Hummels, C. B., Smith, B. D., Hopkins, P. F., et al. 2019, *ApJ*, 882, 156
 Jin, S., Trager, S. C., Dalton, G. B., et al. 2024, *MNRAS*, 530, 2688
 Lanzetta, K. M., Bowen, D. V., Tytler, D., & Webb, J. K. 1995, *ApJ*, 442, 538
 Lehner, N., Howk, J. C., Tripp, T. M., et al. 2013, *ApJ*, 770, 138
 Levi, M., Allen, L. E., Raichoor, R. M., et al. 2019, in *Bulletin of the American Astronomical Society*, Vol. 51, 57
 Lilly, S. J., Carollo, C. M., Pipino, A., Renzini, A., & Peng, Y. 2013, *ApJ*, 772, 119
 Lusso, E., Fumagalli, M., Fossati, M., et al. 2019, *MNRAS*, 485, L62
 Marinacci, F., Vogelsberger, M., Pakmor, R., et al. 2018, *MNRAS*, 480, 5113
 Martin, D. C., Darvish, B., Lin, Z., et al. 2023, *Nature Astronomy*, 7, 1390
 Morrison, S., Pieri, M. M., Som, D., & Pérez-Ràfols, I. 2021, *MNRAS*, 506, 5750
 Morrison, S., Som, D., Pieri, M. M., Pérez-Ràfols, I., & Blomqvist, M. 2024, *MNRAS*, 532, 32
 Murphy, M. T., Kacprzak, G. G., Savorgnan, G. A. D., & Carswell, R. F. 2019, *MNRAS*, 482, 3458
 Naiman, J. P., Pillepich, A., Springel, V., et al. 2018, *MNRAS*, 477, 1206
 Nelson, D., Pillepich, A., & et al. in prep.
 Nelson, D., Pillepich, A., Springel, V., et al. 2019, *MNRAS*, 490, 3234
 Nelson, D., Pillepich, A., Springel, V., et al. 2018, *MNRAS*, 475, 624
 Nuñez, E. H., Steidel, C. C., Kirby, E. N., et al. 2024, *ApJ*, 976, 41
 O’Meara, J. M., Lehner, N., Howk, J. C., & Prochaska, J. X. 2021, *AJ*, 161, 45
 Oppenheimer, B. D., Bogdán, Á., Crain, R. A., et al. 2020, *ApJ*, 893, L24
 Pakmor, R., Marinacci, F., & Springel, V. 2014, *ApJ*, 783, L20
 Pérez-Ràfols, I., Font-Ribera, A., Miralda-Escudé, J., et al. 2018, *MNRAS*, 473, 3019
 Pérez-Ràfols, I., Pieri, M. M., Blomqvist, M., et al. 2023, *MNRAS*, 524, 1464
 Péroux, C., Weng, S., Karki, A., et al. 2022, *MNRAS*, 516, 5618
 Pieri, M. M., Bonoli, S., Chaves-Montero, J., et al. 2016, in *SF2A-2016: Proceedings of the Annual meeting of the French Society of Astronomy and Astrophysics*, ed. C. Reylé, J. Richard, L. Cambrésy, M. Deleuil, E. Pécontal, L. Tresse, & I. Vauglin, 259–266
 Pieri, M. M., Frank, S., Weinberg, D. H., Mathur, S., & York, D. G. 2010, *ApJ*, 724, L69
 Pieri, M. M., Martel, H., & Grenon, C. 2007, *ApJ*, 658, 36
 Pieri, M. M., Mortonson, M. J., Frank, S., et al. 2014, *MNRAS*, 441, 1718
 Pillepich, A., Nelson, D., Hernquist, L., et al. 2018a, *MNRAS*, 475, 648
 Pillepich, A., Nelson, D., Springel, V., et al. 2019, *MNRAS*, 490, 3196
 Pillepich, A., Springel, V., Nelson, D., et al. 2018b, *MNRAS*, 473, 4077
 Press, W. H. & Schechter, P. 1974, *ApJ*, 187, 425
 Prochaska, J. X., Herbert-Fort, S., & Wolfe, A. M. 2005, *ApJ*, 635, 123
 Rahmati, A., Pawlik, A. H., Raičević, M., & Schaye, J. 2013, *MNRAS*, 430, 2427
 Scannapieco, E. & Broadhurst, T. 2001, *ApJ*, 549, 28
 Schmidt, M. 1963, *Nature*, 197, 1040
 Shapley, H. & Curtis, H. D. 1921, *Bulletin of the National Research Council*, 2, 171
 Sijacki, D., Vogelsberger, M., Genel, S., et al. 2015, *MNRAS*, 452, 575
 Springel, V., Pakmor, R., Pillepich, A., et al. 2018, *MNRAS*, 475, 676
 Tinsley, B. M. 1980, *Fund. Cosmic Phys.*, 5, 287
 Toomre, A. & Toomre, J. 1972, *ApJ*, 178, 623
 Tornotti, D., Fumagalli, M., Fossati, M., et al. 2025, *Nature Astronomy*
 Torrey, P., Vogelsberger, M., Genel, S., et al. 2014, *MNRAS*, 438, 1985
 Tumlinson, J., Peebles, M. S., & Werk, J. K. 2017, *ARA&A*, 55, 389
 Vogelsberger, M., Genel, S., Sijacki, D., et al. 2013, *MNRAS*, 436, 3031
 Vogelsberger, M., Genel, S., Springel, V., et al. 2014a, *Nature*, 509, 177
 Vogelsberger, M., Genel, S., Springel, V., et al. 2014b, *MNRAS*, 444, 1518
 Weinberg, D. H., Davé, R., Katz, N., & Kollmeier, J. A. 2003, in *American Institute of Physics Conference Series*, Vol. 666, The Emergence of Cosmic Structure, ed. S. H. Holt & C. S. Reynolds (AIP), 157–169
 Weinberger, R., Springel, V., Hernquist, L., et al. 2017, *MNRAS*, 465, 3291
 Weng, S., Péroux, C., Karki, A., et al. 2023, *MNRAS*, 519, 931
 Weng, S., Péroux, C., Ramesh, R., et al. 2024, *MNRAS*, 527, 3494
 Wolfe, A. M., Gawiser, E., & Prochaska, J. X. 2005, *ARA&A*, 43, 861
 York, D. G., Adelman, J., Anderson, John E., J., et al. 2000, *AJ*, 120, 1579

³ <http://www.astropy.org>

Appendix A: SBLA Counts, P_{tot} and Incidence Rates

In this section, we show the results from the matching of the SBLA positions within the halos, as described in Sect. 3. We also calculated the incidence rate of SBLAs.

From observations, we have incidence rates estimated from 130 SQUAD (Murphy et al. 2019) QSO spectra. At $z = 2$, we have a redshift path length of 0.6, while at $z = 3$ we have 1.4. A cut in signal-to-noise (S/N) in each pixel was applied, where we enforce S/N per pixel > 10 , and also rebinned and smoothed the spectra to match the SDSS 2-pixel rebin wavelength solution, and we ended with 44 QSOs. Then, we divided the data in two redshift bins: one between $1.8 < z < 2.2$ and another between $2.8 < z < 3.2$. We also have access to 150 KODIAQ (O’Meara et al. 2021) QSO spectra. The same cut in S/N was applied, as well as the same rebin and smoothing so the wavelength solution is the same as SDSS 2-pixel rebin, leaving us with 73 QSO spectra. The data was then divided in two redshift bins: $2.15 < z < 2.42$ and $2.8 < z < 3.5$. The incidence rates of both SQUAD and KODIAQ spectra can be found in A.1. All DLAs and sub-DLAs were masked.

For the simulations, we define the incidence rate as:

$$\frac{dn}{dz} = \frac{\text{Number of SBLAs detected}}{\text{Wavelength Interval [\AA]} \cdot \text{Number of lines-of-sight}} \quad (\text{A.1})$$

where the wavelength interval is either 50 Å or 60 Å for $z = 2$ and $z = 3$, respectively, and the number of lines-of-sight is 4 million, minus the DLA sightlines (see Sect. 2). The results of this can be seen in Table A.2 for SDSS-like SBLAs and Table A.3 for variable SBLA sizes, for all redshifts, alongside all the probabilities and SBLA counts mentioned in the main text.

Table A.1. Incidence rates estimated from SQUAD and KODIAQ spectra. The spectra were smoothed and rebinned to be identical to the SDSS 2-pixel wavelength solution.

SQUAD $F_{Ly\alpha}$	$1.8 < z < 2.2$ dn/dz	$2.8 < z < 3.2$ dn/dz
[0.15, 0.25)	3.4 ± 0.47	10.9 ± 1.1
[0.05, 0.15)	2.7 ± 0.43	11.3 ± 1.1
< 0.05	1.1 ± 0.26	4.7 ± 0.71
KODIAQ $F_{Ly\alpha}$	$2.15 < z < 2.42$ dn/dz	$2.8 < z < 3.5$ dn/dz
[0.15, 0.25)	8.41 ± 1.7	14.2 ± 2.3
[0.05, 0.15)	4.4 ± 1.7	7.0 ± 1.8
< 0.05	2.0 ± 1.2	1.6 ± 0.9

Comparing the results from Tables A.1 and A.2, we can see that there is a clear difference between them. Observations have higher incidence rates for all cases, with a difference of up to two orders of magnitude (in the $z = 2$ and $F_{Ly\alpha} < 0.05$ case). The differences are much less stark at $z = 3$, with a maximum difference of 2 times between the simulation and the observations.

This is a potential flag that there might be some issues in the generation of the spectra in the TNG50 simulation, as, for example, there could be difficulties in handling the transition between linear to non-linear structure formation at higher redshifts. On the other hand, although the SQUAD spectra have high signal-to-noise, there are still some noise effects – strong absorption

could be slightly over/underestimated and SBLAs could be put in the ‘wrong’ $F_{Ly\alpha}$ bin, boosting the dn/dz estimation of one bin and reducing the other.

Appendix B: Variable SBLA Spectral Size in the Non-Hierarchical Framework

In this section, we show the results of the $P(M_h)$ and C_{frac} for the variable SBLAs in the non-hierarchical framework, in Figs B.1 and B.2, respectively.

Table A.2. Total number of SBLAs, n_{SBLA} , the respective probability of finding them in halos, P_{tot} , as well as the incidence rate, dn/dz , for each redshift in the TNG50 simulation box. This is presented for the SDSS case described in Sect. 4.

v_{SBLA} [km s $^{-1}$]	$F_{\text{Ly}\alpha}$	$z = 2$			$z = 3$		
		n_{SBLA}	P_{tot}	dn/dz	n_{SBLA}	P_{tot}	dn/dz
SDSS 138	< 0.25	153633	0.56	0.95	2477078	0.17	13.22
	< 0.15	34931	0.65	0.22	871377	0.27	4.65
	< 0.05	1372	0.78	0.01	132918	0.42	0.71

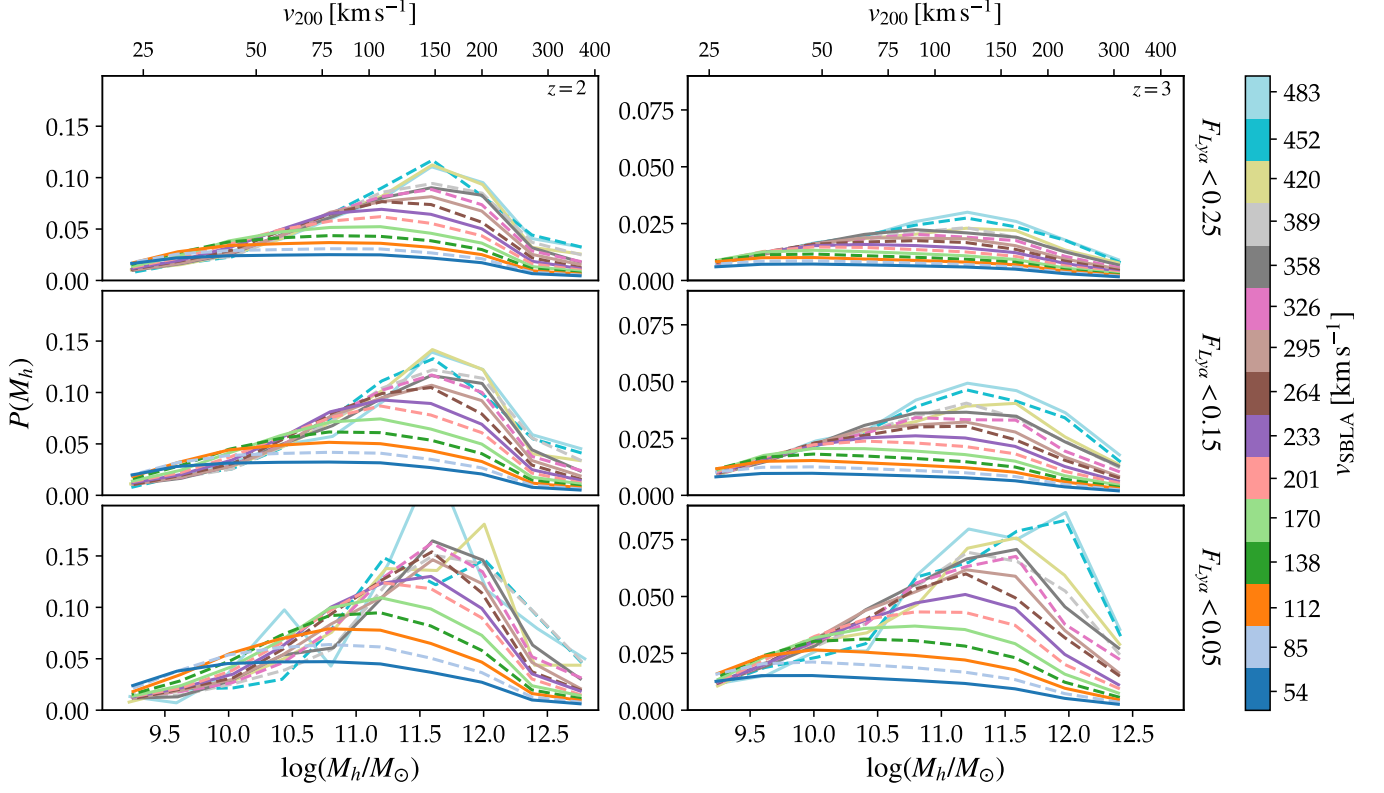


Fig. B.1. $P(M_h)$ without using the hierarchical framework. $z = 2$ results are on the left panels and $z = 3$ results are on the right. All remaining elements are the same as in Fig. 5.

Table A.3. Total number of SBLAs, n_{SBLA} , the respective probability of finding them in halos, P_{tot} , for each redshift in the TNG50 simulation box. We also consider the hierarchical framework, by simply adding a subscript h to the counter, e.g. $n_{h,\text{SBLA}}$, and we calculate the incidence rate, dn/dz , for these SBLAs. This is presented for the resolved spectra case described in Sect. 5.

v_{SBLA} [km s ⁻¹]	$F_{L_{\text{Ly}\alpha}}$	$z = 2$					$z = 3$				
		n_{SBLA}	P_{tot}	$n_{h,\text{SBLA}}$	$P_{h,\text{tot}}$	dn/dz	n_{SBLA}	P_{tot}	$n_{h,\text{SBLA}}$	$P_{h,\text{tot}}$	dn/dz
54	< 0.25	13268521	0.18	3310301	0.05	20.54	45253628	0.05	8729618	0.0	46.6
	< 0.15	9501758	0.23	2951002	0.1	18.31	33175144	0.06	8867342	0.01	47.34
	< 0.05	5498951	0.31	2214722	0.19	13.74	19989161	0.1	7360312	0.03	39.29
85	< 0.25	6597498	0.22	1650782	0.09	10.24	23867995	0.06	4301141	0.01	22.96
	< 0.15	4307885	0.28	1324103	0.15	8.22	15866509	0.08	3842303	0.02	20.51
	< 0.05	2163281	0.39	838390	0.28	5.2	8283265	0.13	2727084	0.06	14.56
112	< 0.25	4015923	0.25	1098122	0.13	6.81	15464301	0.07	2912033	0.01	15.55
	< 0.15	2430704	0.33	820123	0.22	5.09	9520623	0.1	2437582	0.04	13.01
	< 0.05	1087094	0.45	464148	0.36	2.88	4438240	0.17	1537354	0.09	8.21
139	< 0.25	2598739	0.29	806626	0.18	5.01	10671222	0.08	2163993	0.02	11.55
	< 0.15	1459972	0.37	551799	0.28	3.42	6113412	0.12	1665131	0.05	8.89
	< 0.05	582547	0.49	276058	0.43	1.71	2573833	0.19	950712	0.13	5.08
170	< 0.25	1634429	0.32	477874	0.22	2.97	7371416	0.09	1592813	0.03	8.5
	< 0.15	853553	0.41	306296	0.33	1.9	3917196	0.13	1150919	0.07	6.14
	< 0.05	303582	0.53	140700	0.47	0.87	1468194	0.22	585543	0.15	3.13
201	< 0.25	1077730	0.35	362331	0.27	2.25	5334243	0.1	1220715	0.04	6.52
	< 0.15	521254	0.44	214384	0.37	1.33	2636842	0.15	802922	0.09	4.29
	< 0.05	162109	0.56	83775	0.53	0.52	886698	0.25	364054	0.2	1.94
233	< 0.25	733287	0.37	244017	0.3	1.51	3929248	0.1	896787	0.05	4.79
	< 0.15	331270	0.46	134240	0.4	0.83	1815055	0.16	558370	0.1	2.98
	< 0.05	93507	0.58	49143	0.55	0.3	553897	0.27	237159	0.21	1.27
264	< 0.25	505709	0.39	170725	0.32	1.06	2985871	0.11	702000	0.06	3.75
	< 0.15	212398	0.49	88452	0.43	0.55	1270738	0.18	396560	0.12	2.12
	< 0.05	52328	0.6	29604	0.57	0.18	341367	0.3	145028	0.25	0.77
295	< 0.25	349131	0.41	111280	0.34	0.69	2324111	0.12	611884	0.08	3.27
	< 0.15	136070	0.5	53649	0.45	0.33	940272	0.19	326311	0.14	1.74
	< 0.05	29649	0.59	16036	0.58	0.1	224879	0.32	102042	0.29	0.54
326	< 0.25	248199	0.43	86552	0.39	0.54	1815778	0.12	423255	0.08	2.26
	< 0.15	89234	0.53	37328	0.49	0.23	687466	0.2	204036	0.15	1.09
	< 0.05	16469	0.62	9050	0.61	0.06	152973	0.33	63194	0.3	0.34
358	< 0.25	188604	0.44	83083	0.38	0.52	1395462	0.13	359335	0.09	1.92
	< 0.15	66244	0.53	36657	0.48	0.23	497217	0.22	167887	0.17	0.9
	< 0.05	11485	0.62	8196	0.58	0.05	97845	0.35	47320	0.34	0.25
389	< 0.25	129532	0.46	64698	0.41	0.4	1172977	0.13	323496	0.09	1.73
	< 0.15	39521	0.57	24340	0.53	0.15	397819	0.21	136631	0.17	0.73
	< 0.05	5088	0.64	3901	0.59	0.02	73651	0.35	37072	0.33	0.2
420	< 0.25	94489	0.48	34099	0.42	0.21	959104	0.14	387986	0.1	2.07
	< 0.15	27132	0.58	12504	0.54	0.08	298735	0.22	144834	0.18	0.77
	< 0.05	3063	0.68	1787	0.62	0.01	43137	0.36	26417	0.34	0.14
452	< 0.25	62988	0.51	43781	0.47	0.27	755731	0.15	328130	0.12	46.6
	< 0.15	16231	0.59	12851	0.55	0.08	232231	0.24	121850	0.21	47.34
	< 0.05	1566	0.67	1381	0.62	0.01	31731	0.38	20606	0.36	0.11
483	< 0.25	53461	0.49	53461	0.49	0.33	600455	0.16	600455	0.16	22.96
	< 0.15	12956	0.59	12956	0.59	0.08	165080	0.26	165080	0.26	20.51
	< 0.05	1260	0.72	1260	0.72	0.01	20027	0.39	20027	0.39	0.11

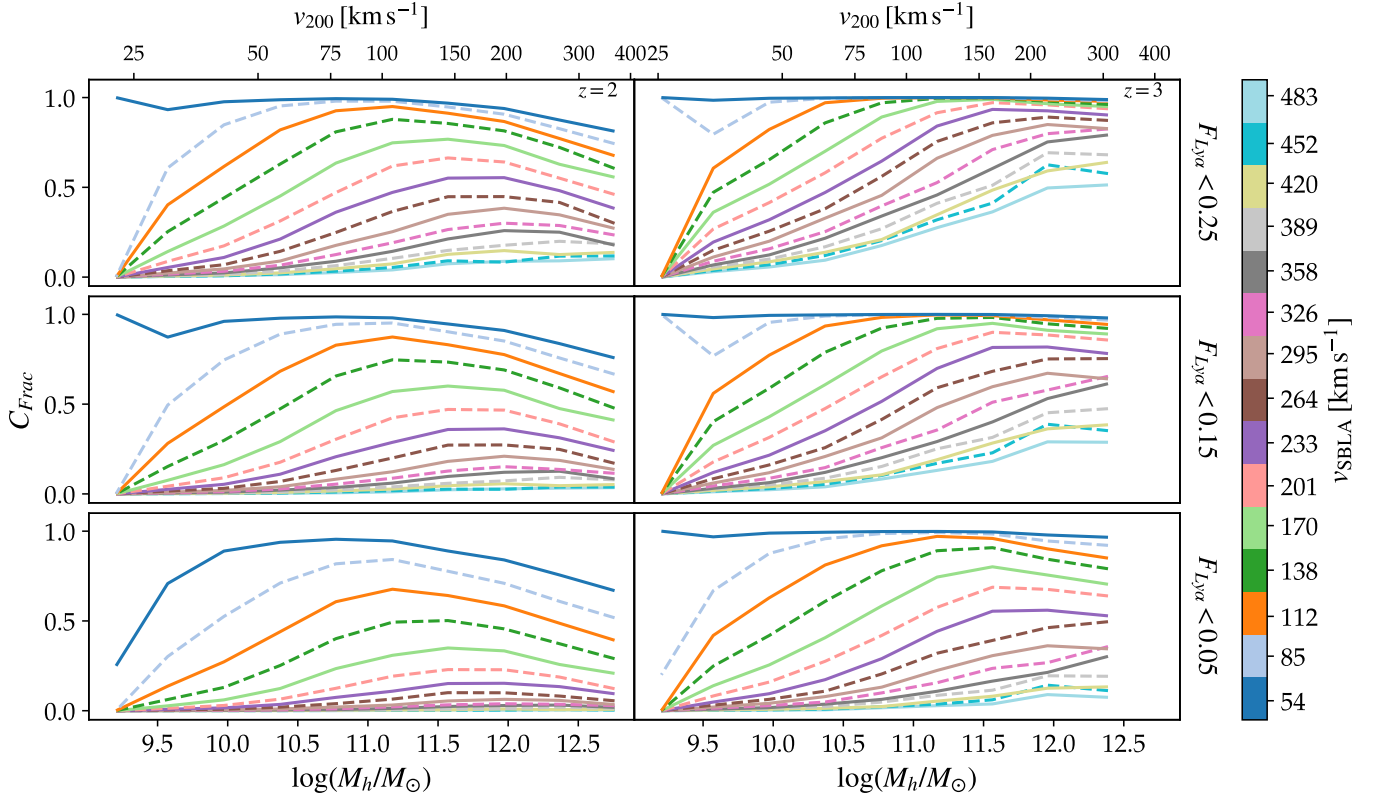


Fig. B.2. Covering fraction without using the hierarchical framework, divided in mass bins. $z = 2$ results are on the left panels and $z = 3$ results are on the right. All remaining elements are the same as in Fig. 5.